# *Precise subcellular functional organization of excitation and inhibition in the direction-selective ganglion cell circuit*

Benjamin L. Murphy-Baum*, Geoff deRosenroll*, Varsha Jain*, Mike Delsey, Kerry Delaney, and Gautam B. Awatramani[§]

Department of Biology, University of Victoria, Victoria, BC, Canada

*These authors contributed equally

[§]Correspondence should be addressed to:

Dr. Gautam Awatramani

Department of Biology
259D Cunningham
University of Victoria
Victoria BC V8W 3N5
Phone: 250-472-5178

Email: gautam@uvic.ca

Author Contributions:

BMB: $Ca^{2+}$ imaging data acquisition, data analysis, writing—original draft, review, and editing. GD: computational modeling, data analysis, writing—review and editing. VJ: $Ca^{2+}$ imaging data acquisition, data analysis, writing—review and editing. MD and KD: $Ca^{2+}$ imaging acquisition hardware, review and editing. GA: supervision, funding acquisition, experimental design, writing—review and editing.

The authors declare no competing interests.

**SUMMARY**

Recent studies indicate that the precise timing and location of inhibition (I) and excitation (E) on the dendritic tree can significantly impact neuronal function. However, the spatiotemporal scale over which synaptic inputs are coordinated and integrated in intact circuits remains unclear. Here, analysis of isolated local light-evoked $Ca^{2+}$ signals in the dendrites of retinal direction-selective ganglion cells reveals that synaptic inputs are integrated within semi-independent micron-scale subunits (<10 µm). Strikingly, each dendritic subunit is well-tuned for direction, indicating that the presynaptic circuitry driving the inhibitory and excitatory inputs known to underlie direction-selective computations is coordinated on a fine spatiotemporal scale. Finally, we show that inhibition can differentially affect activity at dendritic sites even within the same branch, allowing nearby dendrites to relay distinct computational outcomes to the soma. Together, our findings provide new insights into how neurons may compute information rapidly and accurately using parallel processing schemes.

## INTRODUCTION

Neural computations often rely on interactions between excitatory and inhibitory synaptic inputs[1–6]. For neurons with active dendritic trees, nonlinear interactions between excitation and inhibition can have significant consequences on neuronal output. While excitation can recruit regenerative voltage-gated channels and trigger dendritic spikes[7–10], inhibition serves as an opposing force to gate excitatory activity[11–18]. Such interactions between excitation and inhibition (E/I) form the basis for logical 'AND-NOT' dendritic computations[8,19–22]. E/I can be integrated over a range of spatial and temporal scales depending on a number of factors, including the passive cable properties of dendrites, their branching patterns, channel expression patterns, and the strength of ongoing synaptic conductances[23–27]. Recent studies suggest that neurons may be able to integrate synaptic inputs locally and independently—within individual dendrites[28–36]. This enables neurons to process multiple streams of information in parallel, which significantly boosts their computational capacity[37–42].

An important prerequisite for local dendritic computations is that presynaptic inputs be *coordinated* over the same spatiotemporal scale as which they are *integrated* over. While this is often tacitly assumed, experimental evaluation of presynaptic input activity patterns in intact networks remains a central challenge. To this end, retinal direction-selective ganglion cells (DSGCs) have served as a unique model to assess the extent to which excitatory and inhibitory inputs are presynaptically coordinated and postsynaptically integrated. In this circuit, it is well established that asymmetrical inhibition combines with symmetrical excitation to generate robust direction-selective spiking output in DSGCs[43]. While the net directional tuning of the excitatory and inhibitory inputs can be measured at the soma using whole cell recordings (Figure 1A), how the excitatory and inhibitory inputs are functionally distributed within the DSGC's dendritic arbor is unknown and is the main question to be addressed in this study.

Although it is prohibitively difficult to directly measure local E/I at multiple dendritic locations electrophysiologically, several lines of circumstantial evidence suggest that E/I is processed within sub-regions of the DSGC's dendritic tree. Barlow and Levick (1965) first demonstrated that visual stimuli moving over small regions of the DSGC's receptive field generate direction-selective responses, suggesting that the presynaptic circuitry required for the computation is contained within subunits at least as small as ~50-100 µm in diameter[19]. Based on the natural

branching patterns and the theoretical passive voltage length constants of ganglion cell dendrites, Koch et al. (1982) inferred electrically isolated sub-regions of the dendritic tree over which inputs are postsynaptically integrated[13,20]. The Barlow-Levick subunits and the dendritic subunits from Koch et al. appear to be well matched in size, implying that the presynaptic coordination and postsynaptic integration of excitatory and inhibitory inputs are intimately linked ('broad' processing scheme; Figure 1C). However, the spatial scale of direction-selective computations in the dendrites of DSGCs depend on several factors, including the conductance state[23,26,27,33,44] and the presence of nonlinear dendritic conductances[32,41], and remains to be experimentally measured.

Here, in a multi-compartmental network model of a mouse ON-OFF DSGC stimulated with experimentally measured synaptic conductances, we demonstrate that the integration of excitation and inhibition occurs in a spatiotemporally restricted manner ('fine' processing scheme; Figure 1D). During network computations, inputs misplaced by a few microns or mistimed by a few milliseconds did not strongly interact[28–31] and thus synaptic inputs needed to be temporally coordinated at every point in the dendritic tree. If not, local E/I imbalances were amplified by the nonlinear dendritic conductances that have been previously described in these neurons[21,45,46], and degraded the fidelity of the computation.

To experimentally examine the functional organization of E/I in DSGC dendritic arbors, we measured dendritic $Ca^{2+}$ signals using 2-photon imaging. Blocking dendritic voltage-dependent sodium channels ($Na_V$) precluded a direct evaluation of the physiological integrative properties of the cell, but enabled synaptic responses to be evaluated over small sections of dendrite (5-10 μm). Strikingly, under these conditions, dendritic segments distributed throughout the DSGC's dendritic tree were found to be strongly and semi-independently tuned for the direction of object motion, indicating that the presynaptic excitatory and inhibitory inputs are coordinated with exceptionally fine spatiotemporal precision. Together, our findings raise the interesting possibility that neural computations in the brain occur over unprecedentedly small spatial scales, where even single dendritic branches lacking spines may process multiple streams of incoming information in parallel.

## RESULTS

### Fine-scale E/I correlations are critical for accurate and reliable direction selectivity

To understand the impact of E/I coordination on the generation of direction selectivity in DSGCs, we built a multi-compartmental model using the reconstructed morphology of an ON-OFF DSGC[47,48]. Each dendritic site received stochastic inhibitory and excitatory inputs, which were directionally tuned and untuned, respectively. The relative magnitude of the inhibitory and excitatory inputs measured at the soma was similar to that measured experimentally (Figures 1A, 2A). Importantly, the level of spatial ($\rho_s$) and temporal ($\rho_t$) correlation between E/I could be independently varied (see Methods; Figure S1).

The excitatory and inhibitory input currents measured at the soma were similar in correlated ($\rho_s = 0.9$, $\rho_t = 0.9$) and uncorrelated states ($\rho_s = 0$, $\rho_t = 0$). By contrast, the somatic spiking patterns were significantly different under in these two conditions (Figure 2). Specifically, the strength of directional tuning was compromised when the excitatory and inhibitory inputs were uncorrelated (Figure 2A-C, correlated: DSI = 0.55 ± 0.02, uncorrelated: DSI = 0.22 ± 0.02, $p < 0.001$, t-test, n = 20 trials). When we incremented $\rho_s$ and $\rho_t$ individually, we found that correlations in space and time each on their own significantly improved the strength of direction selectivity, and together they had an additive effect (Figure 2D). Moreover, the variance in the preferred angle at the soma (measured as the angular standard deviation, $\sigma_\theta$) was significantly lower when E/I were correlated in both space and time (correlated: $\sigma_\theta = 6.95°$, uncorrelated: $\sigma_\theta = 20.5°$, Angular Distance test, n = 20 trials). Overall, the results from the model suggest that the fidelity of neural computations strongly relies on excitatory and inhibitory synaptic inputs being highly coordinated, both spatially and temporally. It is important to note that in the uncorrelated state, the excitatory and inhibitory inputs still retain some unavoidable temporal correlation from the onset of the stimulus itself. However, our data suggest that further correlation in the release timing and position of E/I is critical for maintaining strong and reliable direction-selective computations.

Since the E/I correlation level affected the tuning properties of the somatic spiking response, but not the somatic currents, the data suggest that E/I correlations are affecting the local dendritic activity. Thus, we examined the tuning properties of individual dendrites. To simplify our analysis and to isolate local synaptic activity, simulations were run in the absence of $Na_V$

channels. Under these conditions, simulated moving edges evoked dendritic postsynaptic potentials (PSPs). Dendritic PSPs comprised smaller, heavily filtered events—representing a global signal from inputs arriving throughout the arbor—and larger, faster events that arise from local synaptic inputs (Figure 3B; Figure S2). Interestingly, in response to null motion, larger voltage deflections were more frequently observed when the excitatory and inhibitory inputs were spatiotemporally uncorrelated (Kolmogorov-Smirnov test, $p < 0.0001$, n = 20 trials from 177 dendritic sites; Figure 3C). Under these conditions, there were many more instances when inhibition failed to oppose excitation across the dendritic tree (Figure 1SF). This significantly weakened the directional tuning in dendrites in the uncorrelated state (correlated: DSI = 0.44 ± 0.15, uncorrelated: DSI = 0.29 ± 0.16; Kolmogorov-Smirnov test, $p < 0.01$, n = 20 trials from 177 dendritic sites; Figure 3D). In addition, there was significantly higher variability in the direction encoded by individual dendrites in the uncorrelated state (correlated: $\sigma_\theta = 28.8 \pm 6.1°$, uncorrelated: $\sigma_\theta = 56.2 \pm 10.0°$, Angular Distance test, $p < 0.01$; Figure 3D-E). Despite differences in variability of the preferred angle, the average direction encoded across the entire arbor was the same in both conditions (Wheeler-Watson test, $p > 0.05$, n = 20 trials from 177 dendritic sites).

Overall, the model data suggest that well-coordinated E/I are critical for maintaining accurate and reliable computations in dendrites, which then impact activity at the soma. In cortical networks, coordinated E/I is usually discussed as a temporal balance, in which inhibition closely tracks excitation with a small temporal delay[3,12] (measured at the soma). Balanced excitatory and inhibitory inputs are thought to drive more precise spike timing[5], sharpen stimulus selectivity[49], and improve coding efficiency across large networks of neurons[3,12]. Similarly, DSGCs also exhibit temporal E/I balance[1], but the present data make it clear that fine *spatial* E/I balance is just as critical for the neuron's functionality.

**Evaluating local synaptic activity using 2-photon $Ca^{2+}$ imaging techniques**

To understand how E/I is coordinated within the real retinal network, we next evaluated dendritic activity patterns in mouse ON-OFF DSGCs using 2-photon $Ca^{2+}$ imaging techniques. Direction-selective $Ca^{2+}$ responses rely on two coincident signals: excitation and directionally-tuned inhibition. Without excitation there is no $Ca^{2+}$ signal, and with inhibition compromised the $Ca^{2+}$ signal is largely non-directional (Figure S3). Thus, in the DSGC circuit, we can use the direction-

selectivity of $Ca^{2+}$ responses as a readout of E/I coordination. Under natural conditions, with voltage-gated sodium channels ($Na_V$) intact, dendritic $Ca^{2+}$ responses reflect the neuron's global activity due to the propagation of dendritic spikes or back-propagation of somatic spikes. Thus, they only provide an estimate of the average E/I coordination throughout the dendritic arbor[45,50] (Figure S4). In order to understand how excitatory and inhibitory inputs are presynaptically coordinated on the scale of dendrites, we needed to record $Ca^{2+}$ signals that arose from local synaptic activity.

To isolate local synaptic activity, DSGCs were loaded with a $Na_V$ blocker (2 mM QX-314, or in some cases 1 µM TTX was included in the bath solution; note presynaptic retinal neurons do not rely on $Na_V$-dependent action potentials for their output) along with $Ca^{2+}$-sensitive and -insensitive indicators (Oregon Green Bapta-1 and Sulforhodamine 101, respectively) through a patch electrode (Figure 4A-B), which was also used to monitor the somatic voltage. Under these conditions, $Ca^{2+}$ influx through voltage-gated $Ca^{2+}$ channels ($Ca_V$) and NMDA receptors provide a readout of local activity. It is important to note that $Ca^{2+}$ signals represent a nonlinear transformation of light-evoked synaptic potentials, even in the absence of $Na_V$ (Figure S5). The nonlinearity of the $Ca^{2+}$ response may help amplify weak differences in voltage arising from changes in E/I, and therefore is ideally suited for measuring E/I coordination[51].

Our first goal was to establish the integrative properties of dendrites in the absence of $Na_V$ activity. Under these conditions, we observed that positive contrast spots drifting across the DSGC's receptive field in the preferred direction evoked robust $Ca^{2+}$ responses throughout the dendritic arbor (Figure 4B-D). The first concrete indication that individual dendrites integrate synaptic input semi-independently came from examining the relative timing onsets of $Ca^{2+}$ signals across the DSGC dendritic tree. $Ca^{2+}$ signals were first observed at dendritic sites located closest to where the moving stimulus entered the DSGC's receptive field (Figure 4C-D). Sites positioned later in the stimulus trajectory had progressively delayed response onsets (Figure 4E-F; Supplemental Movie 1). The stimulus speed, functionally estimated by combining the response latency with the position of the dendritic sites, was 524 ± 28 µm/s (n = 6), close to the actual stimulus speed (500 µm/s). Even in conditions when NMDA receptors were blocked (50 µM D-AP5)—leaving voltage-gated $Ca^{2+}$ channels as the primary source of $Ca^{2+}$ influx—sequential activation of dendritic sites were still observed (n = 3). Since both control and NMDA

receptor block conditions gave similar results, we combined them into the same data set (Figure 4F). From these data, we conclude that the dendritic arbor is not acting as a single unit, but instead processes inputs onto different dendritic branches relatively independently. This argues against the notion that large regions of the dendritic tree are iso-potential (Figure 1C), which would result in more uniform depolarization and similar response latencies throughout the dendritic arbor. It also argues against the idea that NMDA receptors and/or $Ca_V$ channels initiate widespread depolarizations throughout the dendritic tree (i.e. NMDA or $Ca^{2+}$ spikes), at least in the absence of $Na_V$ activity[35,52,53].

Interestingly, while the average latencies of $Ca^{2+}$ signals in different parts of the dendritic tree followed the stimulus velocity, there was considerable variability in the response onsets measured between neighboring branches or even between active sites on a single branch (arrowheads in Figure 4D). This raised the possibility that synaptic inputs may be integrated over smaller dendritic segments. To assess whether dendritic integration occurs at a finer spatial resolution, we measured how dendritic sites co-varied across repeated stimulus trials (Figure 5).

In these experiments, $Ca^{2+}$ signals were extracted from small regions of interest (ROIs; ~3 $\mu m^2$) throughout the dendritic arbor in response to a stimulus moving in a direction orthogonal to the preferred/null axis (Figure 5A). We chose to use orthogonal stimuli because these drive comparable levels of excitation and inhibition, producing intermediate responses with higher trial-to-trial variance (Figure 5B). After subtracting the mean response from individual trials to get the noise residuals, we calculated the correlation strength between the residual responses of each dendritic site and every other site[16] (Figure 5C).

Correlations in the residuals could be measured in neighboring regions of interest, suggesting that those sites were driven by common synaptic input (Figure 5C). Correlations were not apparent when computed on shuffled trials, which was an important internal control for this analysis. Site-to-site correlations rapidly decayed over distance with a space constant $\lambda = 5.3$ µm (Figure 5D-E; n = 6 cells). Since anatomical studies have shown that ON-OFF DSGCs have E/I synapses every ~1-3 µm throughout their dendritic arbor, our data suggest that each dendritic site only integrates information from a handful of synapses[54,55].

An important point to note is that nonlinearities inherent in $Ca^{2+}$ measurements tend to emphasize local synaptic activity, and activity at a given site is not completely independent of

the global activity across the dendritic tree. Our model DSGC indicates that distal inputs are heavily filtered but still likely to contribute to a weak global depolarization (Figure S2). However, it is the faster larger local inputs that are likely to generate dendritic spikes, which makes non-linearities of $Ca^{2+}$ signals an extremely useful feature in the context of understanding non-linear synaptic integration.

**Direction selectivity within small dendritic subunits**

The finding that the excitatory and inhibitory inputs are integrated semi-independently over small subunits raises the question as to whether the presynaptic circuitry can activate the precise amount of inhibition and excitation required to drive direction selectivity at each dendritic subunit. From somatic recordings, we know that the directional tuning of E/I underlies the tuning properties of the DSGC output (Figures 1A, 2A). We reasoned that if E/I was similarly coordinated at every point in the dendritic tree, then individual subunits would be similarly tuned for direction, as shown in our model. Alternatively, it is also possible that the precise E/I ratios vary across different points due to the stochastic nature of transmitter release and/or wiring inconsistencies, which would give rise to heterogenous tuning properties of individual subunits. In this case, the macroscopic tuning properties would only be realized when responses were averaged across the entire tree, as observed for most other feature-selective neurons[56–59].

Figure 6 illustrates the results from experiments in which we measured dendritic $Ca^{2+}$ signals over a large part of the DSGC's dendritic field, evoked by spots moving in 8 different directions (8 directions = 1 stimulus set). The directional tuning properties of individual subunits did not systematically vary along the dendrites, but were heterogeneously distributed across the dendritic tree (Figure 6F-H), supporting the idea that the excitatory and inhibitory inputs are integrated locally. Over single stimulus sets, there was variability in both the strength and angle of directional tuning across the dendritic arbor. Over 7 cells, the preferred direction computed by each dendritic subunit had an angular standard deviation ($\sigma_\theta$) of 48.1° around the cell's average preferred direction across all sites (Figure 6E). Most dendritic sites (89.5%) had DSI > 0.1, and 60.5% of sites had DSI > 0.2 (Figure 6F). Sites with DSI > 0.1 had tuning curves that were significantly directional around the preferred angle, suggesting that the majority of sites were strongly tuned (Rayleigh test for circular uniformity, $p < 0.01$; Figure S6). Figure 6D shows the average tuning curve for sites within different ranges of DSI (n = 7 cells). Interestingly, null

motion evoked larger $Ca^{2+}$ signals for sites with low DSI than those with high DSI ($\Delta F/F = 0.28 \pm 0.12$ versus $0.17 \pm 0.08$, $p < 0.01$, t-test), suggesting that weakly tuned sites receive weaker inhibitory signals. Conversely, high DSI sites had significantly stronger $Ca^{2+}$ responses to preferred motion than those with low DSI ($\Delta F/F = 1.00 \pm 0.29$ versus $0.73 \pm 0.25$, $p < 0.01$, t-test). Thus, low DSI sites had weaker inputs overall, and thus are less likely to strongly contribute to the overall directional tuning of DSGCs.

Variability in the direction encoded by each dendritic site markedly decreased when it was computed from the average of multiple sets of trials, from $\sigma_\theta = 48.1°$ to $\sigma_\theta = 31.6°$, respectively (Figure 6E; Angular Distance Test, $p = 0.0005$). In other words, the average directional tuning of individual sites was more homogenous across the arbor than the tuning calculated from a single stimulus set (Figure 6F). This is attributable to averaging out variability in the release of presynaptic neurotransmitters, and to a lesser extent recording noise (i.e. PMT multiplication noise; Figure S7). Much of the remaining variability could be due to expected variance in the tuning properties of the presynaptic inhibitory input[16,55], suggesting that the level of E/I delivered to dendritic sites is exceptionally precise.

Figure 6G-H shows high resolution color maps of the peak $\Delta F/F$ in preferred and null directions, the DSI, and the preferred direction, along with the corresponding time varying signals measured over four regions of interest. These data qualitatively illustrate the independent tuning properties of a single dendritic branch, which had no intervening branch points. For example, in Figure 6H, site 1 has highly divergent tuning from its neighbors, largely due to strong $Ca^{2+}$ signals in response to motion at 270° and 315°, which are relatively close to the null direction for this cell. Only 10-20 µm away, sites 2 and 3 had different patterns of activity, with strong responses limited to the 45-135° range, close to the cell's preferred direction. As mentioned earlier, the average tuning of these sites was much more similar, suggesting that differences in tuning on single stimulus sets is the result of variations in local excitatory and inhibitory activity. Since dendritic $Ca^{2+}$ responses were independent within single dendritic branches (Figures 5), and significant variance in directional tuning was present on single branches (Figure 6), the data support the conclusion that E/I is coordinated on an extremely fine spatial scales.

At first glance, the highly compartmentalized dendritic $Ca^{2+}$ responses are surprising, since single dendritic branches are expected to be isopotential. However, we found that in our model,

applying various voltage thresholds to the data strongly impacted the apparent independence of individual dendritic sites, similar to previous descriptions of amacrine cell dendrites[32,41]. Since dendritic action potentials rely on the activation of $Ca_V$ and $Na_V$, which become steeply dependent on voltage above -55 mV[60], we examined how dendritic tuning varies when responses are thresholded in this range. We found that systematically thresholding the voltage data from -55 mV to -48 mV led to an increase in angular variance and DSI ($\sigma_\theta$/DSI = 25.4°/0.42, 40.4°/0.70, and 45.0°/0.80 for -55 mV, -50 mV, and -48 mV thresholds, respectively; Figure S8). When responses were strongly thresholded, even sites located on neighboring branches encoded different directions, indicating their functional independence (Figure 6I-J). Together, the model data indicate that nonlinear processing promotes independence between dendritic branches. If DSGC dendrites receive well-coordinated excitatory and inhibitory inputs, nonlinear integration could allow these small regions of dendrite to shape direction-selective spike output from DSGCs, without requiring integration over larger sections of the arbor.

**Local integration of E/I shapes spiking output**

As an alternate method for measuring the spatial dimensions over which E/I interact, we used a colliding bar stimulus paradigm to drive varying levels of E/I onto different parts of the dendritic tree. In this experiment, we first examined dendritic $Ca^{2+}$ signals in response to a preferred bar alone (150 x 20 µm bar), which primarily drives a wave of excitation across its dendritic tree (Figure 4C). We then asked how these responses were modulated by a null bar presented simultaneously, which drives a wave of activity that is dominated by inhibition (Figure 7A). In these experiments we observed that $Ca^{2+}$ signals were maximally suppressed by the null bar at centrally located dendrites, where the E/I wavefronts generated by the two bars are expected to collide (Figure 7B).

However, the suppression of $Ca^{2+}$ signals by null bar did not occur uniformly across the dendrite, supporting the idea that DSGCs integrate E/I locally (Figure 7B-F). To examine the spatial extent of inhibition, we examined single dendrites orientated along the preferred-null axis, where the effects of the null bar transitioned from weak to strong suppression (Figure 7C-D). We measured line profiles of the peak $Ca^{2+}$ signal along these transition dendrites, and computed the suppression induced by the null bar (Figure 7E). On average, transitions from low levels of suppression to high levels of suppression occurred with a space constant of 8.8 µm (exponential

fit; Figure 7F). These data support our previous results that small dendritic regions are capable of independent signal processing, in that inhibition can have dramatically different impacts on the $Ca^{2+}$ response across closely spaced dendritic sites.

Importantly, when extracellular spikes were measured during collisions, we found that the presence of the null bar produced a narrow window of suppression (Figure 7G-H). The spiking response before and after the inhibitory window was remarkably unaffected. Together, this suggested that even in the context of active dendritic $Na_V$ conductances, the excitatory and inhibitory conductances interact over relatively small distances (Figure 7I), consistent with results from our $Ca^{2+}$ imaging experiments (Figure 5, 6, 7F).

## DISCUSSION

Since the theoretical studies of Rall (1962), there has been broad interest in understanding the role of dendrites in neural processing[61]. Being the receiving units of neural information, dendrites are well positioned to perform complex computations on their inputs that are critical for behavior, especially with regard to sensory systems[39]. Over the last few decades, studies using a variety of state-of-the-art technologies, such as 2-photon glutamate uncaging, have revealed the importance of the spatiotemporal sequence of excitation in dendritic computations[33–36,62,63]. However, understanding how the spatiotemporal patterns of excitatory and inhibitory synaptic activity contribute to ongoing computations at the level of single dendrites has been challenging.

Previous studies investigating E/I coupling in intact networks relied on electrophysiological measurements made from the soma[1–6], which provide little indication of the underlying spatiotemporal patterns of E/I across the dendritic tree. More recent studies have applied innovative methodologies such as multi-site GABA/glutamate iontophoresis or uncaging[28–30,64,65], correlative optical and electrophysiological measurements of spontaneous activity[66], or electrical stimulation of pairs of excitatory and inhibitory neurons[31,65] to investigate subcellular E/I interactions. However, since the integrative properties heavily depend on the conductance state of the neuron[26,27,33,44], the sparse artificial stimulus paradigms used in these *in vitro* studies only provide a limited view of how E/I interact under natural conditions.

By contrast, in this study we show that when DSGCs are stimulated by moving stimuli, the excitatory and inhibitory inputs that underlie direction-selective computations in DSGCs[67] are functionally coordinated on spatial scales of 5-10 µm within single dendritic branches. Thus, E/I interactions appear to occur over an unprecedentedly small spatiotemporal window during natural patterns of synaptic activity. It should be noted that directional tuning by itself does not necessarily indicate E/I coordination. In other sensory circuits small sections of dendrites exhibit distinct feature selectivities—such as tone frequency in neurons of the auditory cortex[68], edge orientation in the visual cortex[57,58], and whisker movement in somatosensory cortex[69]. However, in these cases the dendritic feature selectivity appears to be inherited from already-tuned excitatory inputs[59]. By contrast, feature selectivity in DSGC dendrites relies on the relative strength of the excitatory and inhibitory inputs (Figure S3) and is thus reflective of a postsynaptic dendritic computation.

The cellular mechanisms underlying spatiotemporal coordination can be explained by the well-described properties of the DS circuit. First, single starburst amacrine cell varicosities, which are the presynaptic release sites for GABA onto DSGC dendrites, exhibit robust direction-selective $Ca^{2+}$ responses[16,70,71]. The current study extends these results to suggest that the GABA release from each starburst varicosity is also graded, and drives direction-selective inhibitory conductances at each synaptic contact across the dendritic arbors of DSGCs. Importantly, compromising GABA release from starbursts results in non-directional dendritic $Ca^{2+}$ responses[72], indicating that it is indeed inhibition that shapes excitation at each site throughout the dendritic tree (Figure S3). Not only is it important that GABA be released at each excitatory site, but also that it is precisely timed with excitation, especially for null-direction stimuli where it needs to completely veto excitation. To this end, the known co-transmission of excitatory acetylcholine and GABA neurotransmitters[73,74] from starburst amacrine cells may simplify the task of E/I coordination by minimizing E/I temporal differences and providing a potential substrate for fine-scale spatial coordination. There is growing evidence supporting the idea of acetylcholine /GABA co-transmission in many parts of the brain[75,76], suggesting that this may be a common strategy to produce finely coordinated E/I.

What are the functional consequences of having small computational subunits in dendrites? At first pass, it may seem that coordinating E/I over small dendritic subunits would be of little

significance in the context of active dendritic $Na_V$ conductances, which could potentially spread activity throughout the dendritic tree. However, results from our study indicate that dendritic integration occurs over a narrow spatiotemporal scale in the context of such nonlinear dendritic channels. First, in our simulations, subtle changes in the patterns of E/I had a significant impact on both the dendritic voltage and the somatic spiking output (Figures 2-3). Second, the spike output of real DSGCs could be suppressed by null motion over a narrow temporal window (Figure 7). If synaptic integration occurred over a broad spatiotemporal scale in the context of $Na_V$ activity, we would expect that subtle changes in the patterns of activity would be less consequential, and inhibitory inputs would suppress larger sections of the dendritic arbor for longer durations than what we observed. Moreover, dendritic nonlinearities such as back-propagating spikes serve as a brief signal to rapidly reset the membrane potential, and prepare dendritic segments for receiving new incoming information[21] as the stimulus edge traverses the receptive field. Additionally, several other factors such as voltage-clamping by the somatic firing mechanism, which minimizes NMDA receptor-mediated 'DC cross-talk' between branches, may also contribute to establishing the independence of dendritic subunits[32].

The small 5-10 µm dendritic subunits described here likely represent a minimum estimate of the integrative subunit for DSGC dendrites, since they were measured under optimal stimulation conditions. In more complex visual environments, where the conductances are weaker or less uniform across the dendritic tree, E/I integration may be expected to occur over larger areas. Or even during preferred motion, in which there is very little inhibitory conductance at all, integration may occur over larger domains. In addition, as the dendritic tree tapers towards the distal terminal branches, it is also possible that the integration occurs in a hierarchical fashion as described for rabbit ON DSGCs[21]. Here, dendritic "spikelets" formed in multiple fine terminal dendritic branches act cooperatively to increase the probability of dendritic spike initiation in common parent dendrites. While this hierarchical scheme may entail larger integrative subunits, the important implication of our study is that E/I would be appropriately coordinated at every point of the tree, even at the level of single terminal branches, and thus improve the fidelity of the computation.

The finding that E/I is coordinated and integrated semi-independently within small sections of single dendritic branches challenges the notion that single branches are the basic computational

units of neurons[34–36,61,77,78]. This may provide several computational advantages. First, the subunit structure greatly improves both the spatial and temporal resolution of the computation. For example small computational subunits could provide the substrate for motion hyperacuity where micron-scale stimuli movements drive direction-selective spiking[79]. In the temporal domain, small subunits allow DSGCs to continuously relay directional information to higher visual centers as the stimulus traverses its receptive field, which may be highly beneficial in the natural environment, in which the direction of moving objects if often changing. Furthermore, complex patterns of activity on different parts of the dendritic arbor can be evaluated relatively independently and may have important consequences for how DSGCs process motion information content in a more complex visual environment, as demonstrated by our 'colliding bar' experiment.

Overall, the present study gains a deeper understanding of the local interactions of excitatory and inhibitory inputs in dendrites, and how they shape neural computations. Previous work has discussed computations occurring on the level of networks of neurons[3], single neurons[37], and single dendritic branches[7,80]. Here, our data raise the possibility that multiple, semi-independent E/I computations are carried out even within a single dendritic branch and highlight the computational benefits of point-to-point E/I interactions. Interestingly, recent evidence suggests that direction selective neurons in the cortex also may rely on E/I interactions[22], similar to what has been described in retina. Whether single neurons in cortical circuits have similarly tight spatial and temporal E/I coordination in order to prevent errant dendritic spiking remains to be determined. The recent advent of tools to optically monitor dendritic excitation and inhibition (iGluSnFR[81] and iGABASnFR[82], respectively) paves the way for exciting future investigations of how inhibition and excitation shape direction selectivity and other neural computations carried out by diverse circuits in the brain.

## METHODS

### *Animals*

Experiments were performed using adult (P30 or older) mice of either sex: C57BL/6J (RRID: IMSR_JAX:000664), Trhr-EGFP (RRID: MMRRC_030036_UCD), or Hb9-EGFP (RRID: MGI_109160). Animals were housed in 12-hour light/dark cycles, in up to 5 animals per cage.

All procedures were performed in accordance with the Canadian Council on Animal Care and approved by the University of Victoria's Animal Care Committee.

*Tissue preparation*

Mice were dark-adapted for at least 45 minutes before being anesthetized with isoflurane and decapitated. Retinas of both eyes were extracted in standard Ringer's solution under a dissecting microscope equipped with infrared optics. Isolated retinas were laid flat, ganglion cell side up, over a pre-cut window in 0.22 mm membrane filter paper (Millipore). Mounted retinas were placed into a recording chamber and perfused with Ringer's solution (110 mM NaCl, 2.5 mM KCl, 1mM $CaCl_2$, 1.6 mM $MgCl_2$, 10 mM glucose, 22 mM $NaHCO_3$) heated to 35°C and bubbled with 95% $CO_2$/5% $O_2$. Retinas were illuminated with infrared light and visualized with a Spot RT3 CCD camera (Diagnostic Instruments) through a 40x water-immersion objective on a BX-51 WI microscope (Olympus Canada).

*Visual Stimulation*

Visual stimuli were produced using a digital light projector and were focused onto the photoreceptor layer of the retina through the sub-stage condenser. The background luminance was measured to be 10 photoisomerisations/s (R*/s). Moving stimuli were designed and generated using a custom stimulus design and presentation GUI (StimGen) in either a MATLAB environment with Psychtoolbox or in a python environment with PsychoPy (https://github.com/benmurphybaum/StimGen).

*Electrophysiology*

DSGCs were identified using 2-photon imaging in mouse lines with fluorescent labeling or were identified functionally in wild type mice. Electrodes were pulled from borosilicate glass capillaries to a resistance 3-5 MΩ. For extracellular recordings, electrodes were filled with Ringer's solution. For voltage clamp recordings, electrodes contained the following in mM: 112.5 $CH_3CsO_3S$, 7.75 CsCl, 1 $MgSO_4$, 10 EGTA, 10 HEPES, 5 QX-314-bromide (Tocris). For $Ca^{2+}$ imaging current clamp recordings, electrodes were filled with the following in mM: 115 K-Gluconate, 7.7 KCl, 10 HEPES, 1 $MgCl_2$, 2 ATP-$Na_2$, 1 GTP-Na, 5 phosphocreatine, 2 QX-314, 0.2 Oregon Green Bapta-1, and 0.05 Sulphorhodamine 101. For some recordings, QX-314 was omitted and 1 µM TTX in the bath solution instead. Signals were sampled at 10 kHz and filtered at 2 kHz in a MultiClamp 700B amplifier (Molecular Devices). Analysis was performed using custom routines in MATLAB (Mathworks) and Igor Pro (Wavemetrics). The following pharmacological agents were added directly to the superfusion solution: DL-AP4 (50 µM; Tocris Bioscience), D-AP5 (50 µM; Abcam Biochemicals), UBP-310 (10 µM; Abcam Biochemicals), TTX (1 µM; Abcam Biochemicals), CNQX (20 µM; Tocris Bioscience).

*Calcium Imaging*

For $Ca^{2+}$ imaging experiments, DSGCs were patch clamped in current clamp mode and filled with the calcium indicator Oregon Green Bapta-1 (0.2 mM; ThermoFisher Scientific). For some experiments, a $Ca^{2+}$-insensitive red dye, Sulforhodamine 101 (50 µM; ThermoFisher Scientific), was also included to help visualize the dendritic arbor. After waiting 15-20 minutes for the indicator to fill the dendrites, the microscope was focused onto the ON-stratifying dendritic

layer. 2-photon excitation was delivered using an Insight DeepSee$^+$ laser (Spectra Physics) tuned to 920 nm, guided by XY galvanometer mirrors (Cambridge Technology). Image scans were acquired at 10-15 Hz, or 30 Hz for high speed scans, using custom software developed by Dr. Jamie Boyd (University of British Columbia) in the Igor Pro environment (http://svn.igorexchange.com/viewvc/packages/twoPhoton/).

The laser power was rapidly modulated using a Pockels cell (Conoptics), such that laser power was extinguished during mirror flyback phases but was turned on during data acquisition phases. A counterphase signal was used to turn on and off the projector LEDs during flyback and scan phases, respectively. This method prevents the bright projector light from contaminating the fluorescence signal from the $Ca^{2+}$ indicator, and also minimizes the time that the tissue is exposed to the laser.

PMT single photon currents were converted to voltages with a decay time constant of approximately 250 microseconds. These voltages were digitally sampled at a rate of 40 MHz, integrated for 1 microsecond through a custom time-integrating circuit (designed by Mike Delsey and Kerry Delaney, University of Victoria). This circuit outputs an analog voltage which was then digitized at 1 MHz (PCI-6110, National Instruments) for image formation. This helped decrease fluctuations in signal amplitude that arise from the asynchronous arrival times of single photons during the 1 microsecond dwell time at each image pixel, thereby improving signal to noise at low light levels characteristic of sparse synaptic activity.

*Computational Modeling*

A multi-compartmental model was coded in the NEURON environment[48]. 177 pairs of excitatory and inhibitory synaptic inputs were distributed across the dendritic arbor of a reconstructed ON-OFF DSGC[47]. Membrane capacitance and axial resistance were set to 1 $\mu F/cm^2$ and 100 $\Omega \cdot cm$ respectively. Membrane channels and noise were modeled using a stochastic Hodgkin and Huxley distributed mechanism. Non-voltage-gated leak conductances were set to reverse at -60 mV. Active membrane conductances were placed at the soma, primary dendrites and terminal dendrites with the following densities in $mS/cm^2$ (soma/primary dendrites/terminal dendrites): sodium (150/200/30), potassium rectifier (35/35/25), delayed rectifier (0.8/0.8/0.8). This enabled the model DSGC to process inputs actively via dendritic sodium spikes. Sodium and potassium conductances were blocked for voltage-clamp recordings.

The membrane potential of 700 compartments across the dendritic arbor were recorded in response to a simulated edge moving across the receptive field at 1 mm/s. Mean onset times of each synaptic site were determined by the time at which the simulated edge passed over it. Around these mean onset times, three forms of variation were introduced (Figure S1A-B). First, an upstream shared variation was applied to both excitatory and inhibitory onset times as a simplified analog of light response timing jitter (i.e. photoreceptor jitter, Figure S1B). Subsequently, two distinct forms of variability were then introduced to control the level of spatial or temporal correlation between excitation and inhibition. Spatial correlations were set by linking the probability of synaptic release at inhibitory/excitatory synapses that are activated at each point of the dendritic tree as the simulated bar passes over them. High spatial correlations mean that if inhibitory transmitter is released, it is more likely that excitatory transmitter will also be released at that point in the dendritic tree (vice versa).

To correlate transmitter release of excitation and inhibition, the variable, I, is selected randomly from a Gaussian distribution centered around zero. If this value is within specified limits of the distribution, there will be successful synaptic release of inhibition (green area in Figure S1C). The limits defining successful or unsuccessful release depend on the direction of motion, with more stringent limits during preferred motion when the probability of release is low, and broader limits during null motion when the probability of release is high. The release probability for excitatory synapses was held constant across all directions (Figure S1E). Release of excitatory neurotransmitter is correlated with that of inhibition through the equation:

$$E = I \cdot \rho_s + \sqrt{1 - {\rho_s}^2} \cdot R \tag{1}$$

Where $\rho_s$ is the correlation coefficient between E and I, and R is a value pulled from a Gaussian distribution centered around zero. The resulting value of E amounts to a weighted sum of the values pulled from the I and R distributions. For instance, if $\rho_s = 1$, E and I reduce to the same value, whereas if $\rho_s = 0$, E and I are completely independent. Similar to inhibition, if the resulting value of E falls within specified limits of the distribution, there will be successful excitatory release. This procedure was performed for every pair of E/I synapses in the dendritic arbor, where $\rho$ represents the spatial correlation between excitation and inhibition. The same procedure was carried out for the timing of synaptic release for each pair of excitatory and inhibitory inputs, where $\rho_t$ represents the temporal correlation between excitation and inhibition:

$$E = I \cdot \rho_t + \sqrt{1 - {\rho_t}^2} \cdot R \tag{2}$$

For the release timing, an unshared temporal variation was added to the E and I onset times.

The correlations were accurately reflected in the distributions of possible onset times by calculation of the Pearson's R (Figure S1D). As expected, when the correlation between E and I was increased in the null direction, in which inhibitory release is maximal, the proportion of unopposed excitatory events decreased (Figure S1F). For the purposes of this demonstration, unopposed excitation is defined as an excitatory release event that coincides with an inhibitory failure (fully unopposed excitation), or when inhibition lags excitation by more than 1 time constant of the excitatory conductance (partially unopposed excitation).

*Quantification and statistical analysis*

All analysis and statistical comparisons were done using Igor Pro (WaveMetrics). All population data was expressed as mean ± standard error unless otherwise specified. Angular data was expressed as mean ± angular standard deviation ($\sigma_\theta$). The preferred direction and strength of the directional tuning was defined as the vector summation of the component responses for the 8 stimulus directions, which was computed as:

$$R_x = \sum_{i=1}^{n} R_i \cdot \cos\theta_i \tag{3}$$

$$R_y = \sum_{i=1}^{n} R_i \cdot \sin\theta_i \tag{4}$$

$$R_t = \sum_{i=1}^{n} R_i \tag{5}$$

$$\vec{R} = \sqrt{{R_x}^2 + {R_y}^2} \tag{6}$$

$$\vec{\theta} = \tan^{-1}\frac{R_y}{R_x} \tag{7}$$

Where $R$ is the response for the $i$th stimulus direction, $\theta$, $R_x$ and $R_y$ are the $x$ and $y$ component responses, and $R_t$ is the summed total of all responses. $\vec{R}$ and $\vec{\theta}$ are the length of the vector sum and the its angle. The direction selective index (DSI) is computed as the normalized length of the vector sum:

$$DSI = \frac{\sqrt{{R_x}^2+{R_y}^2}}{R_t} \tag{8}$$

The angular standard deviation of a population of angles was calculated as:

$$\sigma_\theta = \sqrt{-2 \cdot \log(V)} \tag{9}$$

where $V = \sqrt{(\sum_{i=1}^{n}\cos\theta_i)^2 + (\sum_{i=1}^{n}\sin\theta_i)^2}$ (10)

and $\theta$ is the $i$th angle in the population.

Statistical comparisons between mean angles were done using the Wheeler-Watson test, and comparisons between the angular variance of two populations were done using the Angular Distance test. Rayleigh tests were used to test for directional uniformity of an angular distribution. Comparisons between the mean DSI over trials were done using the Student's t test, while comparisons of distributions of DSIs (i.e. among many dendritic sites) were done using the Kolmogorov-Smirnov test. All other paired comparisons were done using the Student's t test. All comparisons were done using two-tailed statistical tests. Differences were considered significant for $p < 0.05$.

*Data and Software Availability*

The data analysis code is available upon request from the Lead Contact.

*Contact for reagent and resource sharing:*

Further information and requests for resources and reagents should be directed to, and will be fulfilled by, the Lead Contact, Gautam B. Awatramani (gautam@uvic.ca).

## REFERENCES


1. Cafaro, J. & Rieke, F. Noise correlations improve response fidelity and stimulus encoding. *Nature* **468**, 964–967 (2010).
2. D'amour, J. A. & Froemke, R. C. Inhibitory and excitatory spike-timing-dependent plasticity in the auditory cortex. *Neuron* **86**, 514–528 (2015).
3. Denève, S. & Machens, C. K. Efficient codes and balanced networks. *Nat. Neurosci.* **19**, 375–382 (2016).
4. Rupprecht, P. & Friedrich, R. W. Precise Synaptic Balance in the Zebrafish Homolog of Olfactory Cortex Article Precise Synaptic Balance in the Zebrafish Homolog of Olfactory Cortex. *Neuron*

**100**, 1–15 (2018).
5. Wehr, M. & Zador, A. M. Balance inhibition underlies tuning and sharpens spike timing in auditory cortex. (Supplementary material). *Nature* **426**, 2189 (2003).
6. Xue, M., Atallah, B. V. & Scanziani, M. Equalizing excitation-inhibition ratios across visual cortical neurons. *Nature* **511**, 596–600 (2014).
7. Branco, T. & Häusser, M. Synaptic Integration Gradients in Single Cortical Pyramidal Cell Dendrites. *Neuron* **69**, 885–892 (2011).
8. Major, G., Polsky, A., Denk, W., Schiller, J. & Tank, D. W. Spatiotemporally Graded NMDA Spike / Plateau Potentials in Basal Dendrites of Neocortical Pyramidal Neurons. *J. Neurophysiol.* **99**, 2584–2601 (2008).
9. Gasparini, S. & Magee, J. C. State-Dependent Dendritic Computation in Hippocampal CA1 Pyramidal Neurons. *J. Neurosci.* **26**, 2088–2100 (2006).
10. Schmidt-Hieber, C. *et al.* Active dendritic integration as a mechanism for robust and precise grid cell firing. *Nat. Neurosci.* **20**, 1114–1121 (2017).
11. Grienberger, C., Milstein, A. D., Bittner, K. C., Romani, S. & Magee, J. C. Inhibitory suppression of heterogeneously tuned excitation enhances spatial coding in CA1 place cells. *Nat. Neurosci.* **20**, 417–426 (2017).
12. Isaacson, J. S. & Scanziani, M. How inhibition shapes cortical activity. *Neuron* **72**, 231–243 (2011).
13. Koch, C., Poggio, T. & Torre, V. Retinal Ganglion Cells: A Functional Interpretation of Dendritic Morphology. *Phil. Trans. R. Soc. Lond.* **298**, 227–264 (1982).
14. Murayama, M. *et al.* Dendritic encoding of sensory stimuli controlled by deep cortical interneurons. *Nature* **457**, 1137–1141 (2009).
15. Lovett-Barron, M. *et al.* Regulation of neuronal input transformations by tunable dendritic inhibition. *Nat. Neurosci.* **15**, 423–430 (2012).
16. Poleg-Polsky, A., Ding, H. & Diamond, J. S. Functional Compartmentalization within Starburst Amacrine Cell Dendrites in the Retina. *Cell Rep.* **22**, 2898–2908 (2018).
17. Ranganathan, G. N. *et al.* Active dendritic integration and mixed neocortical network representations during an adaptive sensing behavior. *Nat. Neurosci.* **21**, 1583–150 (2018).
18. Muñoz, W., Tremblay, R., Levenstein, D. & Rudy, B. Layer-specific modulation of neocortical dendritic inhibition during active wakefulness. *Science (80-. ).* **355**, 954–959 (2017).
19. Barlow, H. B. & Levick, W. R. The Mechanism of Directionally Selective Units in Rabbit's Retina. *J. Physiol.* **178**, 477–504 (1965).
20. Schachter, M. J., Oesch, N. W., Smith, R. G. & Rowland Taylor, W. Dendritic spikes amplify the synaptic signal to enhance detection of motion in a simulation of the direction-selective ganglion cell. *PLoS Comput. Biol.* **6**, e1000899 (2010).
21. Sivyer, B. & Williams, S. R. Direction selectivity is computed by active dendritic integration in retinal ganglion cells. *Nat. Neurosci.* **16**, 1848–1856 (2013).
22. Wilson, D. E., Scholl, B. & Fitzpatrick, D. Differential tuning of excitation and inhibition shapes direction selectivity in ferret visual cortex. *Nature* **560**, 97–101 (2018).
23. Rall, W. Theory of Physiological Properties of Dendrites. *Ann. New York Acad. Sci.* 1071–1092 (1962).
24. Rall, W. & Rinzel, J. Branch Input Resistance and Steady Attenuation for Input to One Branch of a Dendritic Neuron Model. *Biophys. J.* **13**, 648–688 (1973).
25. Koch, C., Poggio, T. & Torre, V. Nonlinear interactions in a dendritic tree: Localization, timing, and role in information processing. *Proc. Natl. Acad. Sci.* **80**, 2799–2802 (1983).
26. Bernander, O., Douglas, R. J., Martin, K. A. & Koch, C. Synaptic background activity influences spatiotemporal integration in single pyramidal cells. *PNAS* **88**, 11569–11573 (1991).
27. Williams, S. R. Spatial compartmentalization and functional impact of conductance in pyramidal neurons. *Nat. Neurosci.* **7**, 961–967 (2004).
28. Liu, G. Local structural balance and functional interaction of excitatory and inhibitory synapses in

hippocampal dendrites. *Nat. Neurosci.* **7**, 373–379 (2004).
29. Lowe, G. Inhibition of Backpropagating Action Potentials in Mitral Cell Secondary Dendrites. *J. Neurophysiol.* **88**, 64–85 (2002).
30. Marlin, J. J. & Carter, A. G. GABA-A Receptor Inhibition of Local Calcium Signaling in Spines and Dendrites. **34**, 15898–15911 (2014).
31. Müllner, F. E., Wierenga, C. J. & Bonhoeffer, T. Precision of Inhibition : Dendritic Inhibition by Individual GABAergic Synapses on Hippocampal Pyramidal Cells Is Confined in Space and Time. *Neuron* **87**, 576–589 (2015).
32. Behabadi, B. F. & Mel, B. W. Mechanisms underlying subunit independence in pyramidal neuron dendrites. *PNAS* **111**, 498–503 (2014).
33. Magee, J. C. Dendritic integration of excitatory synaptic input. *Nat. Rev. Neurosci.* **1**, 181–190 (2000).
34. Polsky, A., Mel, B. W. & Schiller, J. Computational subunits in thin dendrites of pyramidal cells. **7**, 621–627 (2004).
35. Schiller, J., Major, G., Koester, H. J. & Schiller, Y. NMDA spikes in basal dendrites of cortical pyramidal neurons. *Nature* **404**, 285–289 (2000).
36. Losonczy, A. & Magee, J. C. Integrative Properties of Radial Oblique Dendrites in Hippocampal CA1 Pyramidal Neurons. *Neuron* **50**, 291–307 (2006).
37. Koch, C. & Segev, I. The role of single neurons in information processing. *Nat. Neurosci.* **3**, 1171–1177 (2000).
38. Larkum, M. E. & Nevian, T. Synaptic clustering by dendritic signalling mechanisms. *Curr. Opin. Neurobiol.* **18**, 321–331 (2008).
39. London, M. & Häusser, M. Dendritic Computation. *Annu. Rev. Neurosci.* **28**, 503–532 (2005).
40. Ujfalussy, B. B., Makara, J. K., Lengyel, M. & Branco, T. Global and Multiplexed Dendritic Computations Under In Vivo-like Conditions. *Neuron* **100**, 579–592 (2018).
41. Grimes, W. N., Zhang, J., Graydon, C. W., Kachar, B. & Diamond, J. S. Retinal Parallel Processors: More than 100 Independent Microcircuits Operate within a Single Interneuron. *Neuron* **65**, 873–885 (2010).
42. Mel, B. W. Synaptic Integration in an Excitable Dendritic Tree. *J. Neurophysiol.* **70**, 1086–1101 (1993).
43. Vaney, D. I. & Taylor, W. R. Direction selectivity in the retina. *Curr. Opin. Neurobiol.* **12**, 405–410 (2002).
44. Häusser, M. Diversity and Dynamics of Dendritic Signaling. *Science (80-. ).* **290**, 739–744 (2000).
45. Oesch, N. W., Euler, T. & Taylor, W. R. Direction-selective dendritic action potentials in rabbit retina. *Neuron* **47**, 739–750 (2005).
46. Trenholm, S. *et al.* Nonlinear dendritic integration of electrical and chemical synaptic inputs drives fine-scale correlations. *Nat. Neurosci.* **17**, 1759–1766 (2014).
47. Poleg-Polsky, A. & Diamond, J. S. NMDA Receptors Multiplicatively Scale Visual Signals and Enhance Directional Motion Discrimination in Retinal Ganglion Cells. *Neuron* **89**, 1277–1290 (2016).
48. Hines, M. L. & Carnevale, N. T. The NEURON Simulation Environment. *Neural Comput.* **9**, 1179–1209 (1997).
49. Wu, G. K., Arbuckle, R., Liu, B.-H., Tao, H. W. & Zhang, L. I. Lateral Sharpening of Cortical Frequency Tuning by Approximately Balanced Inhibition. *Neuron* **58**, 132–143 (2008).
50. Yonehara, K. *et al.* The first stage of cardinal direction selectivity is localized to the dendrites of retinal ganglion cells. *Neuron* **79**, 1078–1085 (2013).
51. DeMill, C. M. & Delaney, K. R. Interaction between facilitation and presynaptic inhibition at the crayfish neuromuscular junction. *J. Exp. Biol.* **208**, 2135–2145 (2005).
52. Larkum, M. E., Zhu, J. J. & Sakmann, B. A new cellular mechanism for coupling inputs arriving at different cortical layers. **398**, 2–5 (1999).
53. Yuste, R., Gutnick, M. J., Saar, D., Delaney, R. & Tank, D. W. $Ca^{2+}$ Accumulations in Dendrites

of Neocortical Pyramidal Neurons : An Apical Band and Evidence for Two Functional Compartments. *Neuron* **13**, 23–43 (1994).
54. Bleckert, A. *et al.* Spatial Relationships between GABAergic and Glutamatergic Synapses on the Dendrites of Distinct Types of Mouse Retinal Ganglion Cells across Development. *PLoS One* **8**, e69612 (2013).
55. Briggman, K. L., Helmstaedter, M. & Denk, W. Wiring specificity in the direction-selectivity circuit of the retina. *Nature* **471**, 183–188 (2011).
56. Meier, M. & Borst, A. Extreme Compartmentalization in a Drosophila Amacrine Cell. *Curr. Biol.* **29**, 1545–1550 (2019).
57. Jia, H., Rochefort, N. L., Chen, X. & Konnerth, A. Dendritic organization of sensory input to cortical neurons in vivo. *Nature* **464**, 1307–1312 (2010).
58. Wilson, D. E., Whitney, D. E., Scholl, B. & Fitzpatrick, D. Orientation selectivity and the functional clustering of synaptic inputs in primary visual cortex. *Nat. Neurosci.* **19**, 1003–1009 (2016).
59. Wertz, A. *et al.* Single-cell–initiated monosynaptic tracing reveals layer-specific cortical network modules. *Science (80-. ).* **349**, 70–74 (2015).
60. Randall, A. D. & Tsien, R. W. Contrasting Biophysical and Pharmacological Properties of T-type and R-type Calcium Channels. *Neuropharmacology* **36**, 879–893 (1997).
61. Stuart, G. J. & Spruston, N. Dendritic integration : 60 years of progress. *Nat. Neurosci.* **18**, 1713–1721 (2015).
62. Williams, S. R. & Stuart, G. J. Dependence of EPSP efficacy on synaptic location in neocortical pyramidal neurons. *Science (80-. ).* **295**, 1907–1910 (2002).
63. Williams, S. R. & Stuart, G. J. Role of dendritic synapse location in the control of action potential output. *Trends Neurosci.* **26**, 147–154 (2003).
64. Hao, J., Wang, X.-D., Dan, Y., Poo, M.-M. & Zhang, X.-H. An arithmetic rule for spatial summation of excitatory and inhibitory inputs in pyramidal neurons. *PNAS* **106**, 21906–21911 (2009).
65. Müller, C., Beck, H., Coulter, D. & Remy, S. Inhibitory Control of Linear and Supralinear Dendritic Excitation in CA1 Pyramidal Neurons. *Neuron* **75**, 851–864 (2012).
66. Takahashi, N., Kobayashi, C., Ishikawa, T. & Ikegaya, Y. Subcellular Imbalances in Synaptic Activity. *Cell Rep.* **14**, 1348–1354 (2016).
67. Taylor, W. R., He, S., Levick, W. R. & Vaney. Retinal Ganglion Cells Dendritic Computation of Direction Selectivity by Retinal Ganglion Cells. *Science (80-. ).* **289**, 2347–2350 (2000).
68. Chen, X., Leischner, U., Rochefort, N. L., Nelken, I. & Konnerth, A. Functional mapping of single spines in cortical neurons in vivo. *Nature* **475**, 501–505 (2011).
69. Varga, Z., Jia, H., Sakmann, B. & Konnerth, A. Dendritic coding of multiple sensory inputs in single cortical neurons in vivo. *Proc. Natl. Acad. Sci.* **108**, 15420–15425 (2011).
70. Koren, D., Grove, J. C. R. & Wei, W. Cross-compartmental Modulation of Dendritic Signals for Retinal Direction Selectivity. *Neuron* **95**, 914-927.e4 (2017).
71. Lee, S. & Zhou, Z. J. The Synaptic Mechanism of Direction Selectivity in Distal Processes of Starburst Amacrine Cells. *Neuron* **51**, 787–799 (2006).
72. Pei, Z. *et al.* Conditional Knock-Out of Vesicular GABA Transporter Gene from Starburst Amacrine Cells Reveals the Contributions of Multiple Synaptic Mechanisms Underlying Direction Selectivity in the Retina. *J. Neurosci.* **35**, 13219–13232 (2015).
73. Lee, S., Kim, K. & Zhou, Z. J. Role of ACh-GABA Cotransmission in Detecting Image Motion and Motion Direction. *Neuron* **68**, 1159–1172 (2010).
74. O'Malley, D. M., Sandell, J. H. & Masland, R. H. Co-release of acetylcholine and GABA by the starburst amacrine cells. *J Neurosci* **12**, 1394–1408 (1992).
75. Granger, A. J., Mulder, N., Saunders, A. & Sabatini, B. L. Cotransmission of acetylcholine and GABA. *Neuropharmacology* **100**, 40–46 (2016).
76. Saunders, A., Granger, A. J. & Sabatini, B. L. Corelease of acetylcholine and GABA from

cholinergic forebrain neurons. *Elife* **4**, e06412 (2015).
77. Cichon, J. & Gan, W.-B. Branch-specific dendritic $Ca^{2+}$ spikes cause persistent synaptic plasticity. *Nature* **520**, 180–185 (2015).
78. Losonczy, A., Makara, J. K. & Magee, J. C. Compartmentalized dendritic plasticity and input feature storage in neurons. *Nature* **452**, 436–441 (2008).
79. Grzywacz, N. M., Amthor, F. R. & Merwine, D. K. Directional hyperacuity in ganglion cells of the rabbit retina. *Vis Neurosci* **11**, 1019–25. (1994).
80. Branco, T. & Häusser, M. The single dendritic branch as a fundamental functional unit in the nervous system. *Curr. Opin. Neurobiol.* **20**, 494–502 (2010).
81. Marvin, J. S. *et al.* An optimized fluorescent probe for visualizing glutamate neurotransmission. *Nat. Methods* **10**, 162–170 (2013).
82. Marvin, J. S. *et al.* A genetically encoded fluorescent sensor for in vivo imaging of GABA. *bioRxiv* (2019).

**FIGURES & LEGENDS**

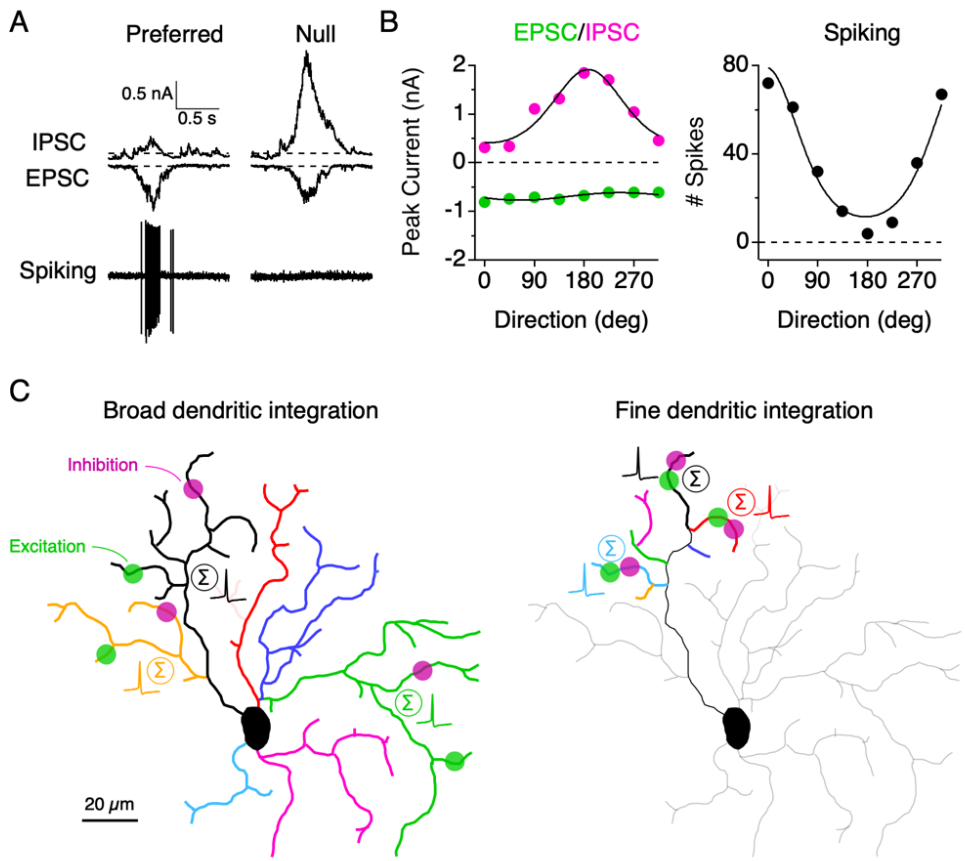


**Figure 1. Mechanisms underlying direction selectivity in retinal ganglion cells. A**, Examples of the excitatory and inhibitory postsynaptic currents (EPSC/IPSCs), and extracellular spikes recorded from an ON-OFF direction selective ganglion cell (DSGC) evoked by a spots moving in its "preferred" or "null" direction. **B**, Variation in the peak amplitudes of the IPSCs and EPSCs, and the number of spikes is plotted against stimulus direction. **C**, EPSCs/IPSCs measured in A are hypothesized to be coordinated and nonlinearly integrated over either a broad (left) or fine spatial scale (right) to ultimately drive direction selectivity in ganglion cells. In the broad integration model, large regions of the dendritic tree are relatively electrically isolated from each other but isopotential within[13,20] (shown in different colors). In this case, presynaptic inputs (excitation, green spots; inhibition, magenta spots) activated over the entire branch structure are integrated to form direction-selective dendritic spikes. By contrast, in the high conductance state, E/I integration may occur over a smaller spatial scale and thus require a finer level of coordination/integration of E/I (right).

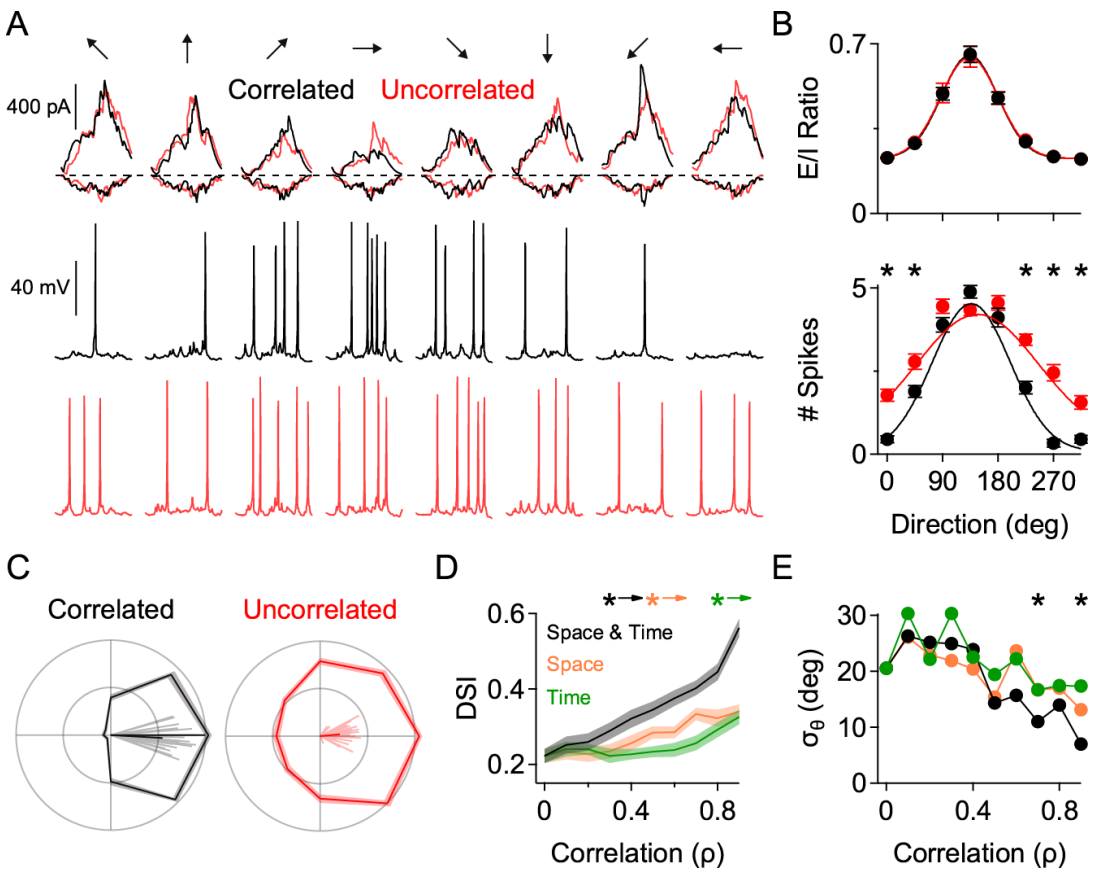


**Figure 2**. **High-fidelity direction encoding relies on precise spatiotemporal coordination of E/I. A**, EPSCs, IPSCs, and somatic spiking for the model DSGC in both correlated ($\rho_s = 0.9$, $\rho_t = 0.9$; black) and uncorrelated ($\rho_s = 0$, $\rho_t = 0$; red) states. **B**, Average E/I ratio (top) and the spike counts (bottom) as a function of direction in correlated (black) and uncorrelated (red) states (n = 20; t-test, $p < 0.05$). Solid lines are Von Mises fits to the data. Note the increase in null spiking in the uncorrelated state. **C**, Polar plots of the somatic spiking response in different states (n = 20). **D**, Direction-selective index (DSI) is plotted as a function of spatial and temporal correlation between the excitatory and inhibitory inputs. The spatial correlation was varied without any temporal correlation (space), vice versa (time), or both were varied together (space + time). * denote $p < 0.05$ (t-test) for comparisons between each data point and the $\rho = 0$ data point for each of the three conditions. Arrows indicate that subsequent data points have also reached significance. **E**, Angular standard deviation of the calculated preferred angle based on somatic spiking, for a range of correlation values. * denote $p < 0.05$ (Angular Distance test).

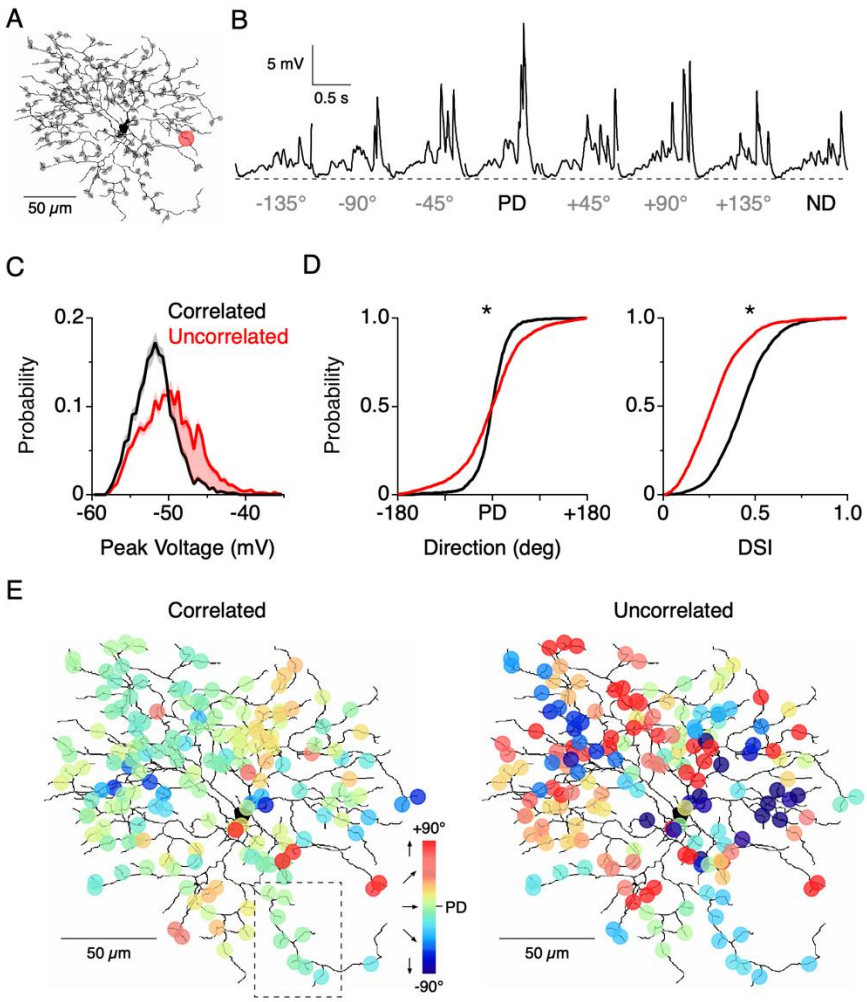


**Figure 3. Spatiotemporal E/I coordination alters dendritic tuning properties.**

**A**, Reconstructed morphology of an ON-OFF DSGC used for the computational model[47] shown in Figure 2. **B**, Simulated light-evoked dendritic voltage responses from a site labeled in **A**. **C**, Histogram of the peak voltage responses evoked during null motion in simulations in which E/I were correlated or uncorrelated. **D**, Cumulative distribution plots of the angle (relative to the preferred direction, PD) and DSI at each dendritic site in different states (n = 20 trials from 177 dendritic sites). * indicates statistical differences between angular variance (Angular Distance test, $p < 0.01$) and DSIs (Kolmogorov-Smirnov test, $p < 0.01$) in the uncorrelated/correlated states. **E**, Spatial maps of the PD in correlated and uncorrelated states, computed from integrated voltage responses (above -55 mV). The demarcated area in **E** is the analyzed dendrite in Figure 6I-J.

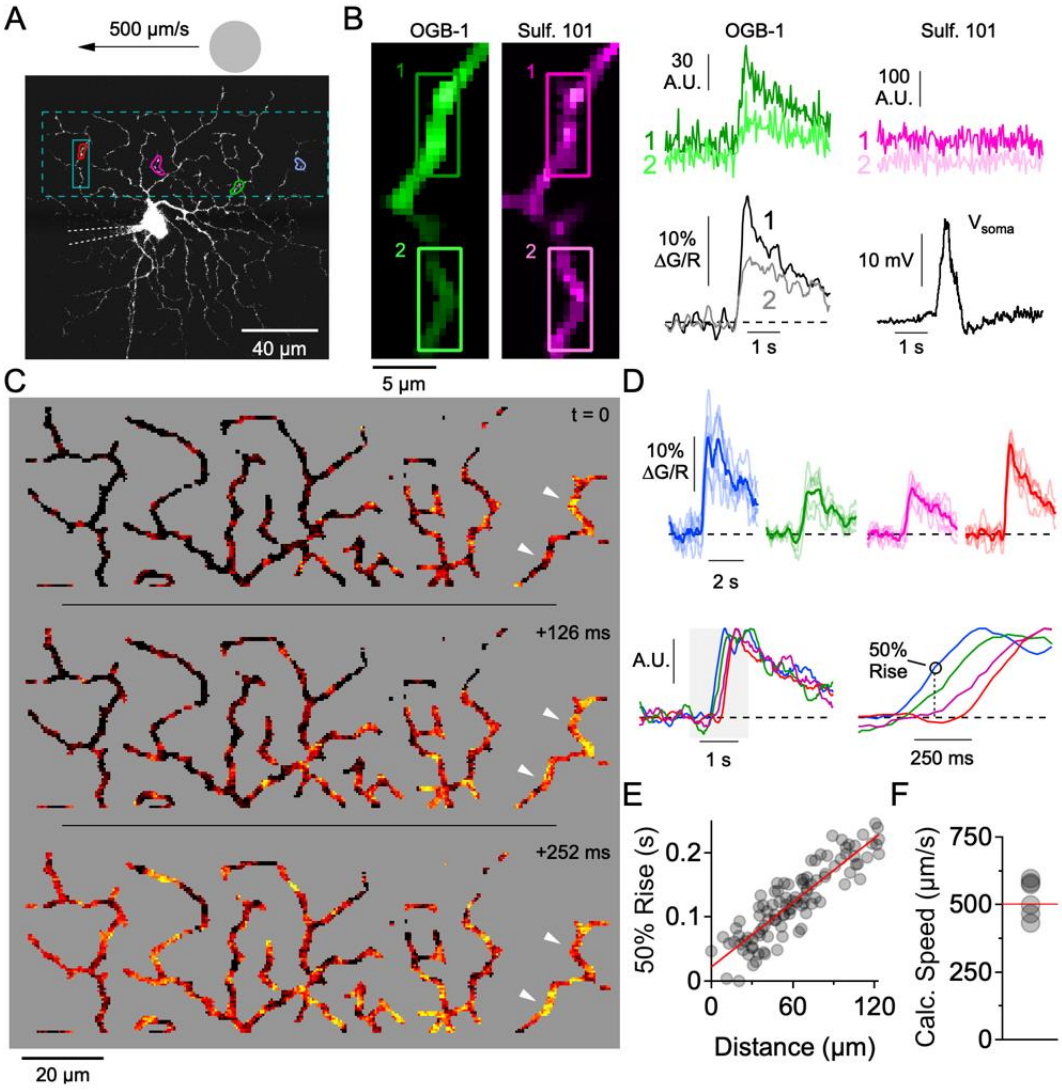


**Figure 4. Sequential activation of individual DSGC dendrites by moving stimuli indicates that they are electrically isolated.**

**A**, 2-photon image of the ON arborization of an ON-OFF DSGC used for $Ca^{2+}$ imaging. The turquoise outlines show the areas analyzed in **B** (small ROI) and **C** (large dashed ROI). The stimulus direction used for **C-G** is indicted above the image. All scans were taken in the presence of $Na_V$ blockers. **B**, Left, 2-photon image of the raw green and red fluorescence during the peak $Ca^{2+}$ response to a moving spot in the preferred direction. Right, time-varying green and red fluorescence counts, the calculated ΔG/R, and the somatic voltage for the two outlined ROIs.

**C**, Single frames of the normalized ΔG/R extracted at different time points from the $Ca^{2+}$ response, showing a characteristic wave of activity that sweeps over the dendritic arbor. Arrowheads mark two areas on a dendrite that have differential response onsets. **D**, Top, individual trials and average ΔG/R for the four colored ROIs outlined in **A**, distributed at different points across the dendritic arbor. Bottom, normalized ΔG/R for the same ROIs, and a zoomed view of the shaded region, showing differential onset timing of $Ca^{2+}$ responses across the dendritic arbor. **E**, 50% rise time for small, 5 $\mu m^2$ ROIs distributed across the dendritic arbor. Only ROIs with responses that reached 2 standard deviations above the baseline noise were used for analysis. **F**, Linear fit to the data in **E** gives an estimate of the stimulus speed (n = 6 cells). Three of these cells were recorded in the presence of the NMDAR antagonist, D-AP5 (50 μM).

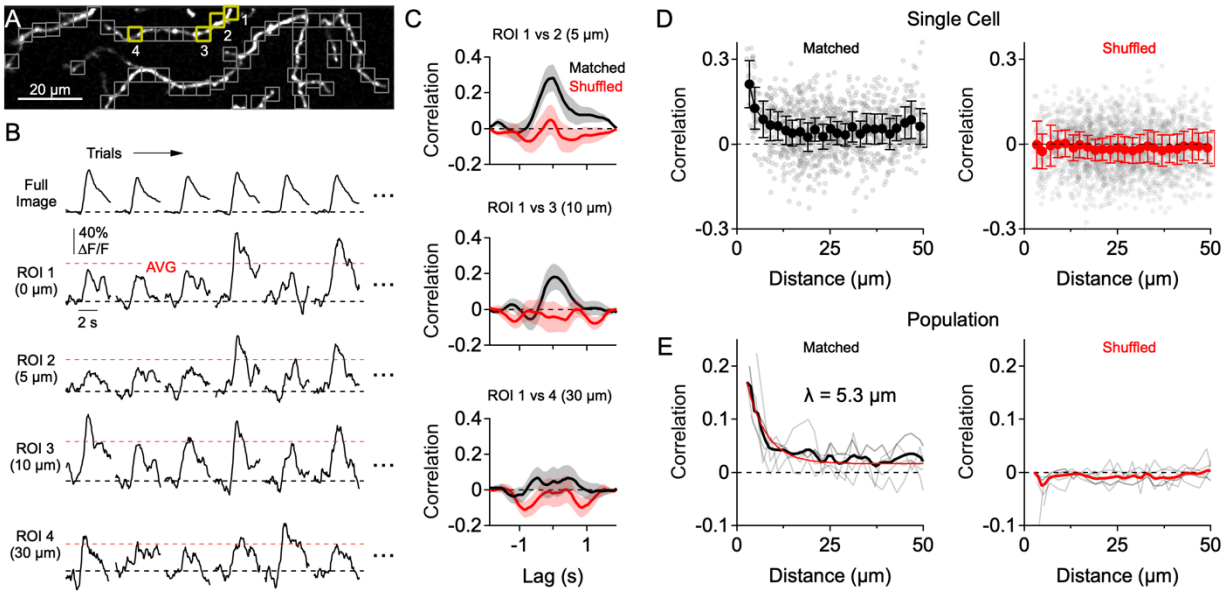


**Figure 5. Noise correlation analysis reveals independent $Ca^{2+}$ responses within small sections of dendrites.**

**A**. 2-photon image of the scan area in the ON arborization of an ON-OFF DSGC, with ROIs throughout the dendritic arbor demarcated in grey, and the ROIs used as examples in yellow. **B**, The average $Ca^{2+}$ signals over the entire arbor (top), and the $Ca^{2+}$ signals from the 4 yellow ROIs in **A** (bottom), from a selection of 6/30 trials obtained for this neuron. Red dotted lines indicate the average peak response over 30 trials. **C**, Cross-correlation of the mean-subtracted residuals from ROI 1 with the 3 other ROIs, each at increasing dendritic distance. Trials were either matched between the ROIs (black) or shuffled (red). **D**, Distance-dependent decay of ROI-ROI correlations with trials either matched (left, black) or shuffled (right, red) for the cell in **A**. The solid black and red data points are binned averages taken every 2 µm from the raw data (grey). **E**, Average distance-dependent decay of ROI-ROI correlations with trials either matched (left, black) or shuffled (right, red) for the population of neurons (n = 6 cells). In matched trials (left), the red line is an exponential fit to the data, with a space constant $\lambda = 5.3$ µm.

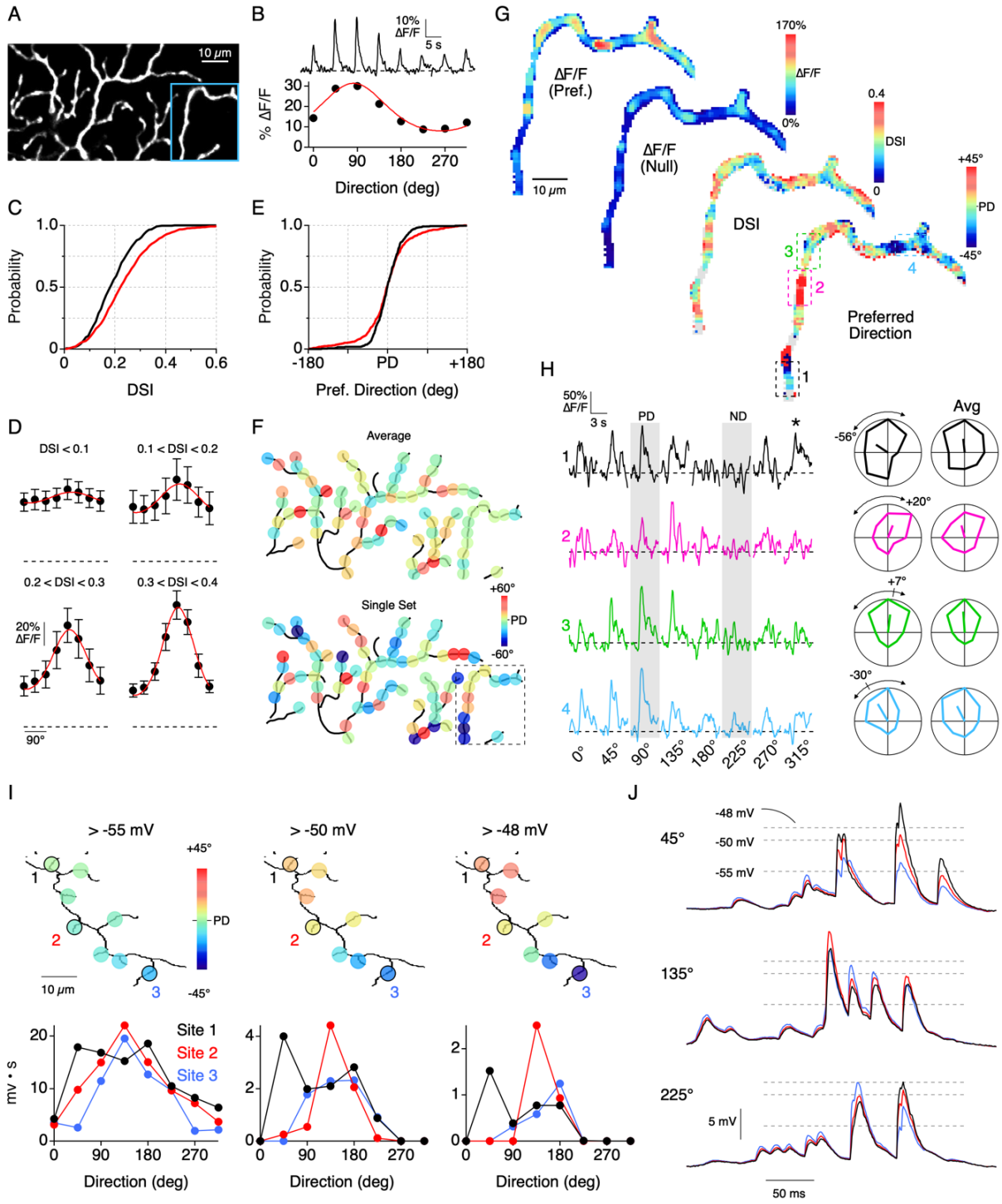


**Figure 6. Directionally-tuned subunits tile the DSGC's dendritic field.**

**Figure 6. Directionally-tuned subunits tile the DSGC's dendritic field.**

**A**, 2-photon image of the scan area in the ON arborization of an ON-OFF DSGC. Turquoise box indicates the area used for analysis in **G-H**. **B**, Dendritic $Ca^{2+}$ signals over the entire imaging area in response to a positive contrast spot moving in 8 different directions (top), and the corresponding tuning curve (bottom). **C**, Cumulative distribution plot of the DSI for a population of 6 neurons measured using responses from a single set of stimuli (red; 8 directions per set), or using each site's average responses over 3 trials (black; n = 6 cells). **D**, The average tuning curve for sites that fell within 4 different ranges of DSI, from low to high. Red lines are Von Mises fits to the data. **E**, Cumulative distribution plot of the calculated preferred direction measured using responses from a single set of stimuli (red), or using each site's average responses over 3 trials (black; n = 6 cells). **F**, The calculated preferred angle at each ROI mapped onto the example DSGC for the 3-trial average, and a single stimulus set (bottom). **G**, High-resolution spatial maps of the peak $\Delta F/F$ for preferred and null stimuli, DSI, and the preferred direction over a single set of 8 stimulus directions. Non-responding pixels were omitted from the DSI and angle maps. **H**, Left, Extracted $Ca^{2+}$ signals from each of the 4 ROIs demarcated in **G** over 8 directions of motion. Right, Polar plots of the directional tuning for the stimulus set used in **G**, as well as the 3-trial average. The neuron's overall preferred (PD) and null directions (ND) are indicated by the grey shading. * marks a strong response to motion close to the null direction, causing that site, but not its neighbors, to have divergent directional tuning. **I**, Top, spatial maps of the preferred direction of the dendritic branch in the demarcated area in **Figure 3E** from the computational model, in which the preferred directions were calculated after thresholding the membrane voltage at different levels. Bottom, directional tuning curves of 3 selected synapses within the branch system. Note the divergence in directional tuning at nearby sites as the threshold becomes more stringent. **J**, Dendritic membrane voltage in response to three different directions of motion for the sites in **I**. Dotted lines indicate the different threshold values used for analysis in **I**.

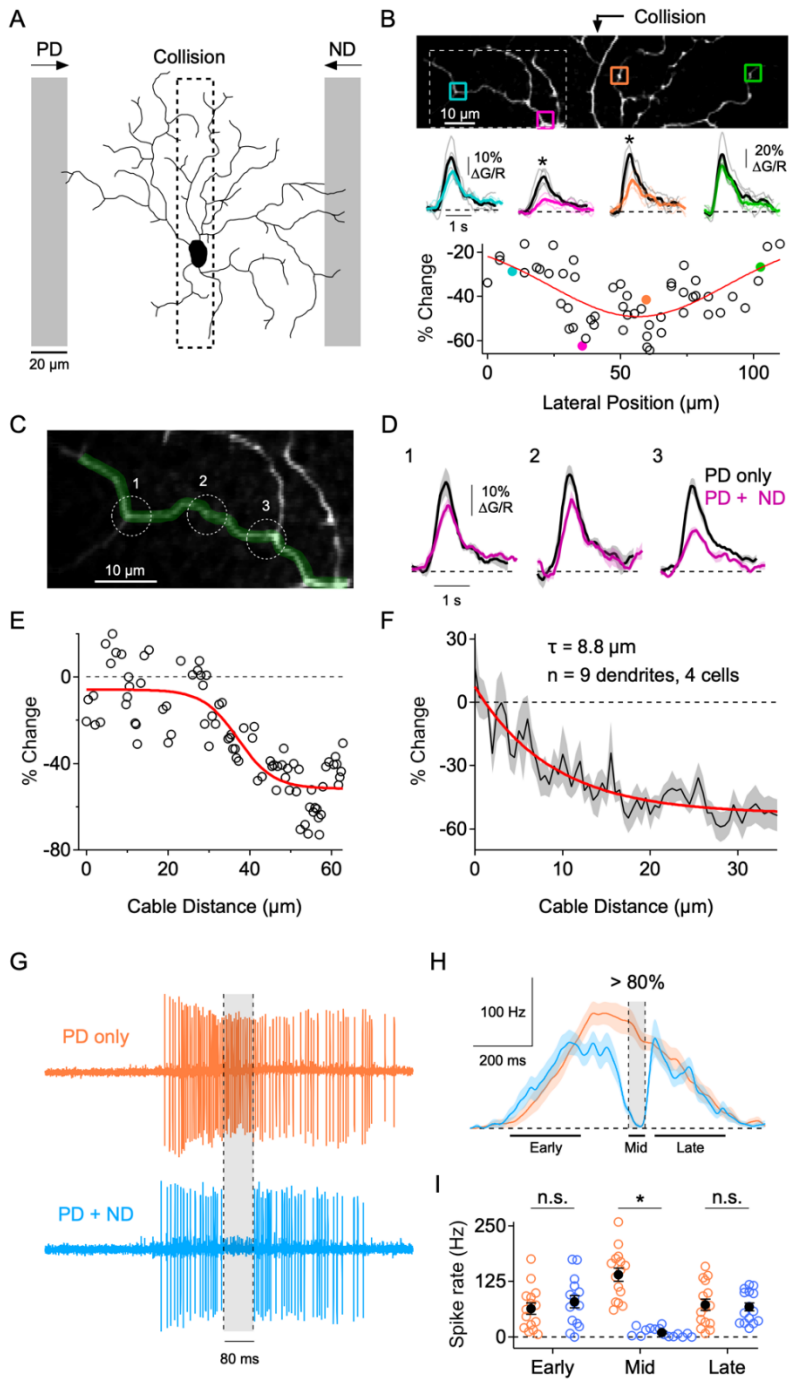


**Figure 7. Collision experiments reveal local coordination and integration of E/I in DSGC dendrites.**

**Figure 7. Collision experiments reveal local coordination and integration of E/I in DSGC dendrites.**

**A**, A narrow (150x20 µm) bar moving in the preferred direction (PD) was presented alone, or simultaneously with a bar moving in the null direction (ND). The dotted box indicates the location of where excitation driven by the PD bar and inhibition driven by the ND bar are expected to coincide. **B**, Top, 2-photon image of the dendritic field of view. ROIs throughout the dendritic arbor are indicated (colored boxes). The white dotted box is the scan area used for line profile analysis in **C**-**F**. Middle, $Ca^{2+}$ signals from the selected ROIs in response to the preferred bar alone (black) or in response to the colliding bars (colored). Bottom, Profile of the change in $Ca^{2+}$ signals at all ROIs as a function of their locations along the preferred-null axis. Red line is a Gaussian fit to the data. **C**, An example of a horizontally orientated 'transition' dendrite, in which the presence of the null bar produces a sharp gradient of inhibition. **D**. Ca responses with and without the null bar in the 3 closely spaced ROIs shown in C. Note that strong suppression of the $Ca^{2+}$ response due to the null bar only occurs in ROI 3. **E**, Percent change due to the presence of the null bar along the line profile demarcated in **C** (green) illustrates the sharp gradient of inhibition in a single dendrite. **F**, Dendrites that showed transitions between strong and weak suppression were aligned and averaged across cells (n = 9 dendrites from 4 cells). The red line is an exponential fit to the data, with a space constant $\lambda = 8.8$ µm. **G**, A colliding null bar produce a narrow window of spike suppression in DSGCs. **H**, Average peri-stimulus time histograms comparing preferred bar only (PD only) and preferred and null bar (PD + ND) stimuli (n = 15 cells). The rapid onset of inhibition and recovery from inhibition indicates that E/I interactions occur over a small region of the dendritic field. **I**, Average spike rates measured before, during, and after the suppression window. Spike rates were only significantly different between the two conditions close to when the preferred and null bars collided (* $p < 0.01$; t-test, n = 15).

## SUPPLEMENATRY FIGURES & LEGENDS

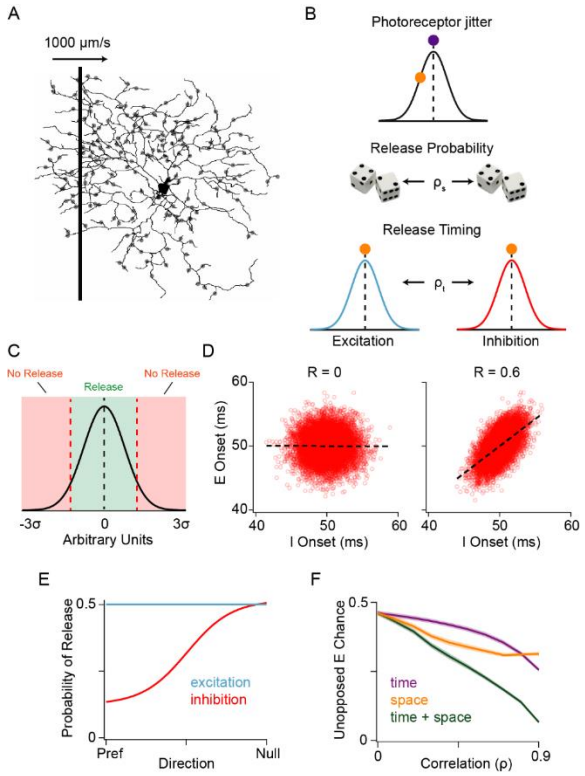


**Figure S1. NEURON model of synaptic input coordination in DSGCs. A**, Reconstruction of an ON-OFF DSGC[47] used for the model. A simulated edge moving across the receptive field is depicted. **B**, Cartoon illustrating the different sources of variability introduced into the model. Spatial and temporal correlations between excitation and inhibition were modulated by adjusting the correlation level of Gaussian distributions, which controlled both the success or failure of vesicle release and the timing of vesicle release for excitation and inhibition. **C**, Values were randomly chosen from Gaussian distribution to determine whether or not each neurotransmitter was released at a given site. Drawn values that fell within defined limits of the distribution triggered successful release. **D**, Plot of onset times of excitation versus inhibition in uncorrelated (left) and correlated (right) states. **E**, Probability of release was altered according to the direction of motion for inhibition, while excitation was non-directional. **F**, Fraction of unopposed excitatory events that happen under a range of spatial and temporal correlation conditions. See Methods for further details.

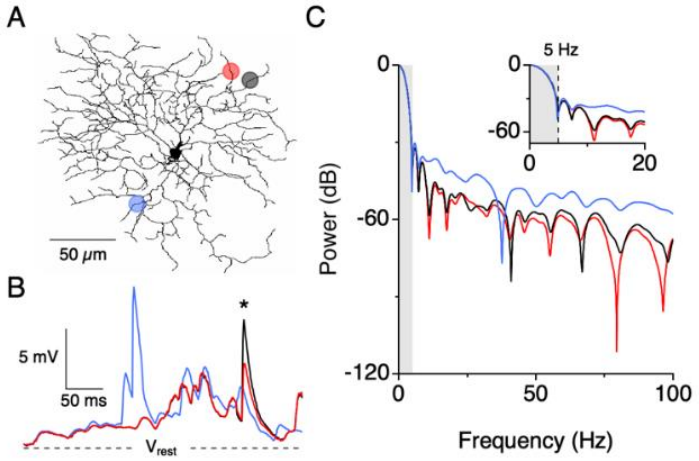


**Figure S2. Strong dendritic filtering of voltage in a model of an ON-OFF DSGC. A**, Two nearby synapses and one distant synapse used for analysis. **B**, Membrane voltage at three sites in response to simulated visual input moving in the preferred direction. Note the strong decay of voltage between the distant site and the two nearby sites. * denotes voltage difference between the nearby sites due to local synaptic input. **C**, Power spectrum of the membrane voltage at the three sites indicated in **A**. Most of the deviation between sites occurs at higher divergent across sites, whereas input that is heavily filtered over long distances is common frequencies, suggesting that the larger, faster inputs that arise from local activity are most among all sites. Inset, zoom-in of the low frequency power spectrum for the three sites.

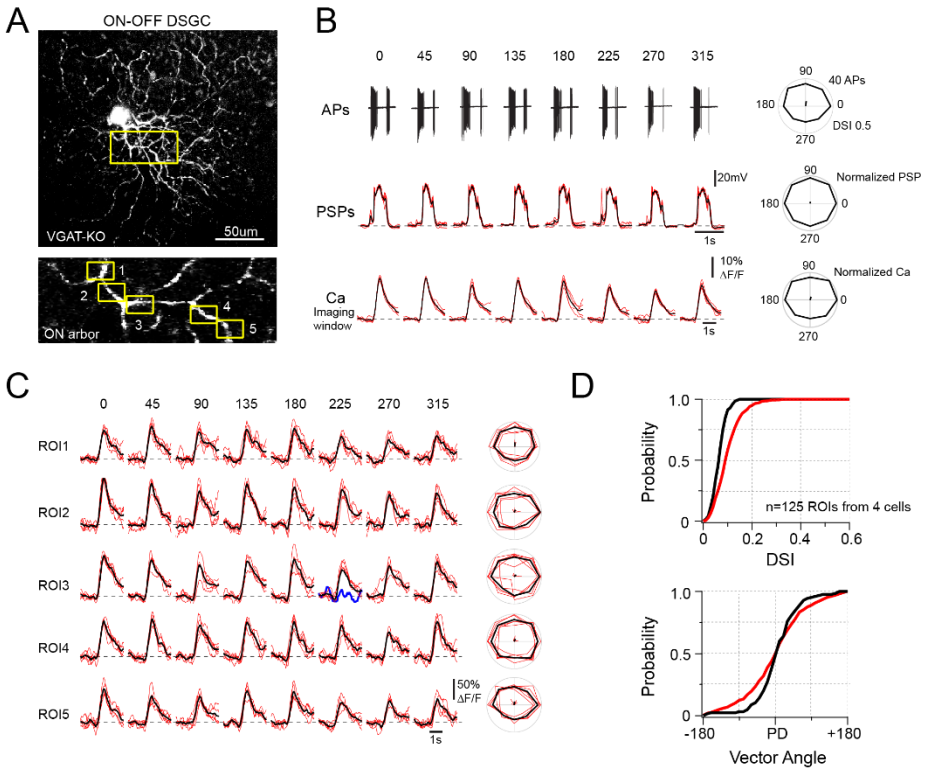


**Figure S3. Non-directional excitation in the absence of directional inhibition.** For these experiments, the vesicular GABA transporter in starburst amacrine cells was knocked out, preventing directionally-tuned GABA release to DSGCs[78]. **A**, 2-photon image of an example ON-OFF DSGC (top), and a zoomed view of the scan area, demarcated in yellow (bottom). **B**, Left, Spikes, post-synaptic potentials (PSPs), and dendritic $Ca^{2+}$ signals over the entire imaging window in response to 200 µm moving spots in 8 directions. Red traces are individual trials, while black traces are the average. Right, Tuning curves of the spikes, PSPs, and $Ca^{2+}$ signals are largely non-directional. **C,** $Ca^{2+}$ responses of 5 ROIs, demarcated in **A**, in response to motion in 8 directions. Right, tuning curves for each of the ROIs. **D,** Top, cumulative distribution of the direction-selective index (DSI) for the dendritic $Ca^{2+}$ signals (n = 4 cells). Note, the vast majority of sites had DSI < 0.1, which is not significantly directional (**Figure S6**). Bottom, cumulative distribution of the preferred angle for dendritic $Ca^{2+}$ signals (n = 4 cells). Black lines use the average $Ca^{2+}$ signals for DSI and preferred angle calculations, whereas the red lines used a single set of trials (eight directions).

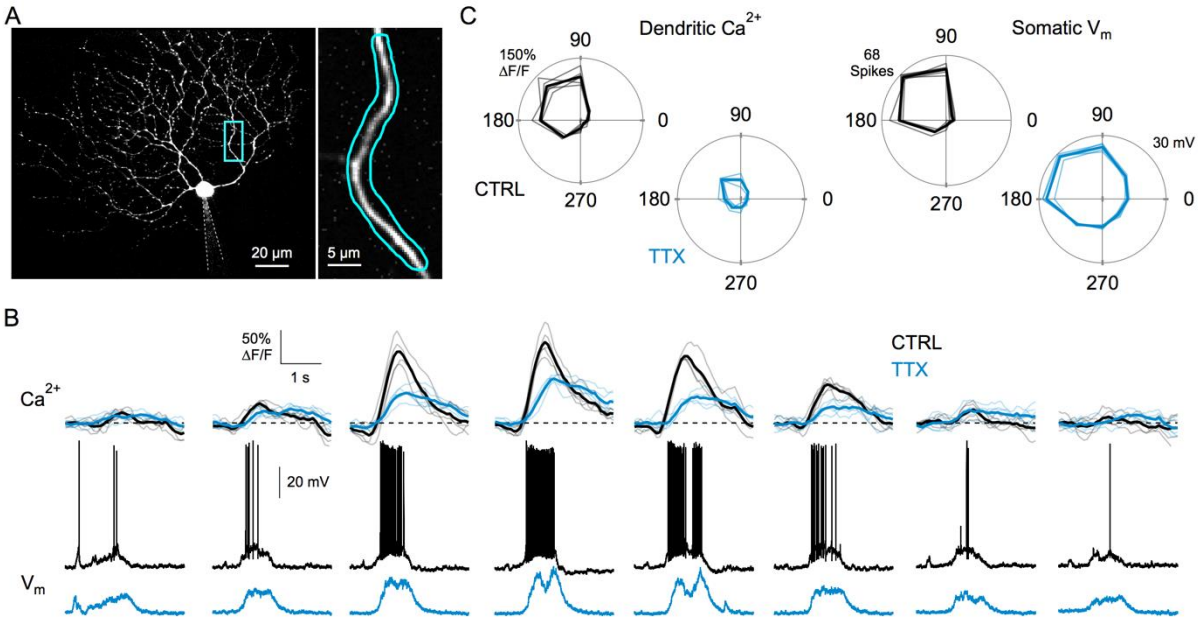


**Figure S4. Dendritic $Ca^{2+}$ signals in the absence of $Na_V$ activity. A**, Left, 2-photon image of a DSGC filled with OGB-1 through a patch electrode. Right, The dendrite used for analysis. **B**, Dendritic $Ca^{2+}$ signals (top) and somatic voltage (bottom), under control conditions (black), and after TTX application (1 µM; turquoise). Thin lines in the $Ca^{2+}$ signals are individual trials, while the thick lines are the average. **C**, Polar plots showing the directional tuning of the dendritic $Ca^{2+}$ signals in control and TTX conditions (left), as well as the number of spikes (control, black) and the amplitude of the subthreshold somatic voltage (TTX, turquoise).

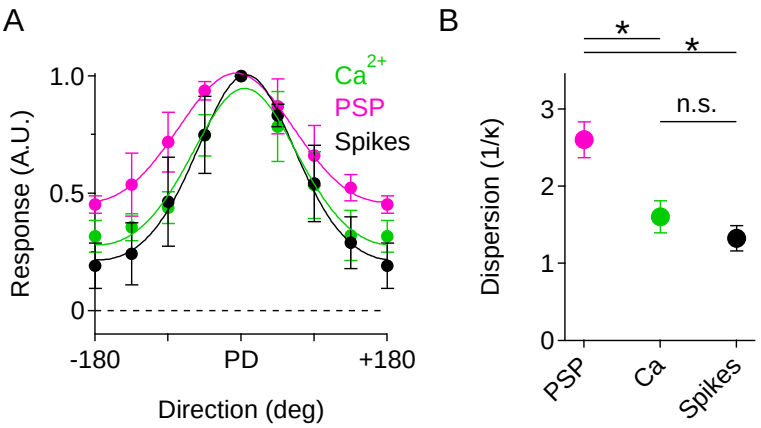


**Figure S5**. **$Ca^{2+}$ measurements and spiking have similar directional tuning properties compared to subthreshold voltage. A**, Directional tuning curves of the somatic spiking response during extracellular recordings (black), subthreshold PSPs under TTX application (magenta), and dendritic $Ca^{2+}$ signals under TTX application (green; n = 6). Solid lines are Von Mises fits to the data. **B**, Angular dispersion of Von Mises fits to the data, expressed as 1/κ, for the three measurement types in **A**. $Ca^{2+}$ signals and spiking both have sharper tuning then the subthreshold PSPs, suggesting that they undergo similar nonlinear thresholding steps.

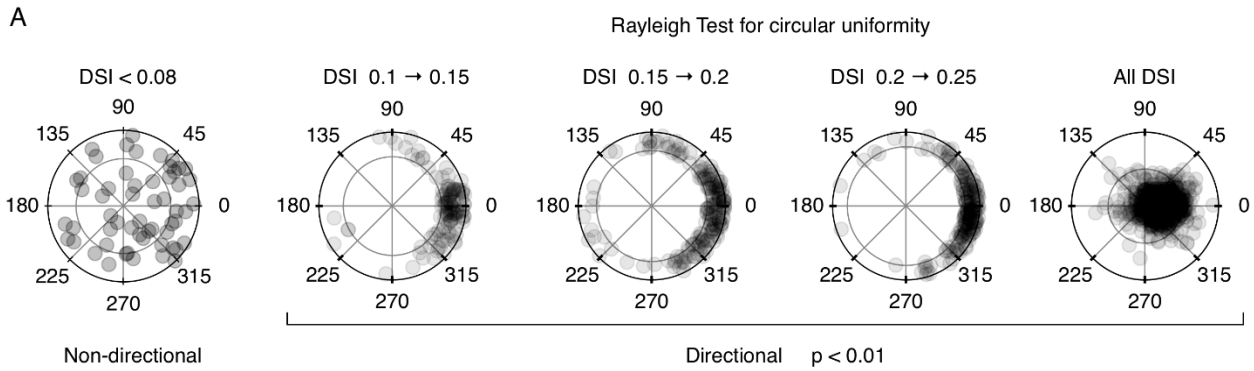


**Figure S6. Strength of directional tuning of dendritic sites. A**, Polar plots of the directional preference of individual dendritic sites that had direction selective indices in specific ranges. Rayleigh tests for circular uniformity were performed on these extracted distributions to test whether each DSI range was tuned to the preferred direction of the DSGC. DSI > 0.1 were significantly directional towards the preferred direction, whereas DSI < 0.1 was nondirectional.

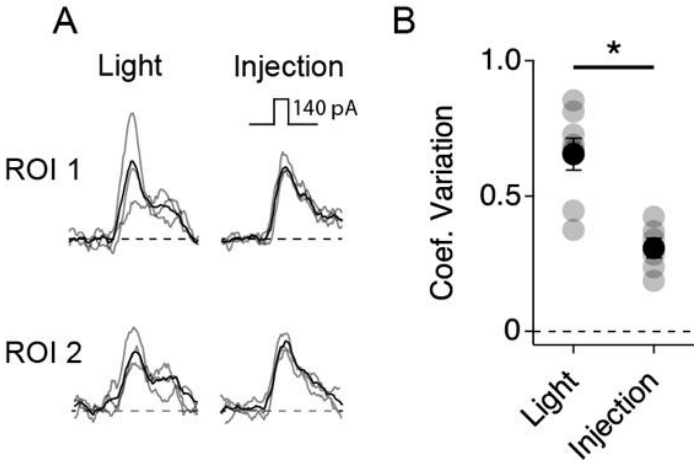


**Figure S7. Variability in $Ca^{2+}$ signals is mostly due to biological noise.** **A**, Example $Ca^{2+}$ signals from two dendritic sites in response to preferred motion and in response to somatic current injection (black average, grey single trials). **B**, Current-injection evoked $Ca^{2+}$ had significantly less variance than light-evoked signals (n= 7 cells), suggesting that most of the light-evoked variance was due to variations in synaptic activity as opposed to instrument noise.

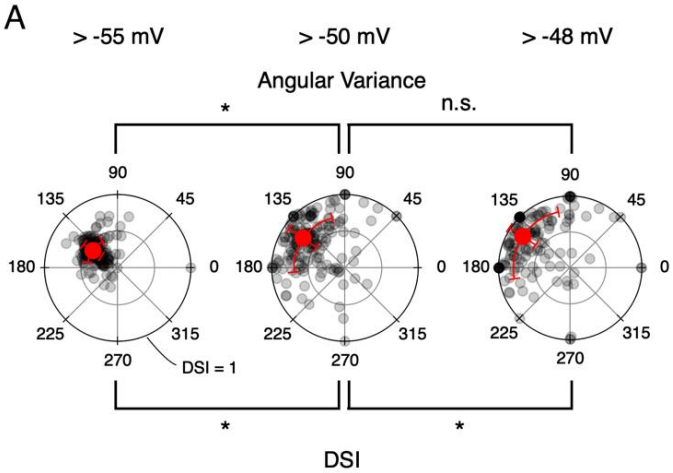


**Figure S8. Nonlinear integration promotes independent computations in dendrites. A**, Polar plots of the preferred angle versus DSI for all dendritic sites in the model DSGC. Data were thresholded at three different levels to show how increasingly stringent voltage thresholding results in significantly larger angular variance (Angular Distance Test) and sharper tuning (larger DSIs; t-test). Asterisks denote $p < 0.05$.